

# Magnetic properties and revisited exchange integrals of the frustrated chain cuprate $\text{PbCuSO}_4(\text{OH})_2$ - linarite

A.U.B. Wolter<sup>1</sup>, F. Lipps<sup>1</sup>, M. Schäpers<sup>1</sup>, S.-L. Drechsler<sup>1</sup>, S. Nishimoto<sup>1</sup>, R. Vogel<sup>1</sup>, V. Kataev<sup>1</sup>,  
B. Büchner<sup>1</sup>, H. Rosner<sup>2</sup>, M. Schmitt<sup>2</sup>, M. Uhlarz<sup>3</sup>, Y. Skourski<sup>3</sup>, J. Wosnitzer<sup>3</sup>, S. Süllow<sup>4</sup>, K.C. Rule<sup>5</sup>

<sup>1</sup>*Leibniz-Institut für Festkörper und Werkstofforschung IFW Dresden,*

*P.O. Box 270116, D-01171 Dresden, Germany*

<sup>2</sup>*Max-Planck-Institut für Chemische Physik fester Stoffe,*

*D-01171 Dresden, Germany*

<sup>3</sup>*Hochfeld-Magnetlabor Dresden (HLD),*

*Dresden-Rossendorf, D-01328 Dresden, Germany*

<sup>4</sup>*Institut für Physik der Kondensierten Materie,*

*TU Braunschweig, D-38106 Braunschweig, Germany*

<sup>5</sup>*Helmholtz-Zentrum Berlin für Materialien und Energie,*

*D-14109 Berlin, Germany*

(Dated: November 23, 2018)

We present a detailed study in the paramagnetic regime of the frustrated  $s = 1/2$  spin-compound linarite,  $\text{PbCuSO}_4(\text{OH})_2$ , with competing ferromagnetic nearest-neighbor and antiferromagnetic next-nearest-neighbor exchange interactions. Our data reveal highly anisotropic values for the saturation field along the crystallographic main directions, with  $\sim 7.6$ ,  $\sim 10.5$  and  $\sim 8.5$  T for the  $a$ ,  $b$ , and  $c$  axes, respectively. In the paramagnetic regime, this behavior is explained mainly by the anisotropy of the  $g$ -factor but leaving room for an easy-axis exchange anisotropy. Within the isotropic  $J_1$ - $J_2$  spin model our experimental data are described by various theoretical approaches yielding values for the exchange interactions  $J_1 \sim -100$  K and  $J_2 \sim 36$  K. These main intrachain exchange integrals are significantly larger as compared to the values derived in two previous studies in the literature and shift the frustration ratio  $\alpha = J_2/|J_1| \approx 0.36$  of linarite closer to the 1D critical point at 0.25. Electron spin resonance (ESR) and nuclear magnetic resonance (NMR) measurements further prove that the static susceptibility is dominated by the intrinsic spin susceptibility. The Knight shift as well as the broadening of the linewidth in ESR and NMR at elevated temperatures indicate a highly frustrated system with the onset of magnetic correlations far above the magnetic ordering temperature  $T_N = 2.75(5)$  K, in agreement with the calculated exchange constants.

PACS numbers: 75.10.Jm, 75.10.Pq, 75.30.Et, 75.30.Gw, 75.30.Kz, 75.40.Cx, 75.50.Ee, 76.30.Fc, 76.60.-k

## I. INTRODUCTION

One-dimensional (1D) quantum magnetism involves the study of materials with magnetic ions of low-spin state,  $s = 1/2$  or 1, which are coupled magnetically along one crystallographic direction only. Due to the rich nature of the low-temperature and field-induced phases in these materials, quasi-1D quantum magnets (Q1DQM) and their effective 1D models have attracted much interest in the last decades from experimentalists and theorists alike.<sup>1-4</sup> Various Q1DQM exhibit highly fascinating field-induced phenomena among which the Bose-Einstein condensation (BEC) of one-magnons (triplons)<sup>5-8</sup> or two-magnon bound states near the saturation field<sup>9,10</sup> are particularly relevant examples. Recent attention has been focussed on the latter phenomenon which is well established for 1D models with competing interactions, where via the inclusion of antiferromagnetic (AFM) next-nearest-neighbor (NNN) interactions magnetic frustration plays a decisive role. A prototype of these systems is the spin  $s = 1/2$  chain with ferromagnetic (FM) nearest-neighbor (NN) and AFM-NNN interactions,

$$\hat{H} = J_1 \sum_l \mathbf{S}_l \cdot \mathbf{S}_{l+1} + J_2 \sum_l \mathbf{S}_l \cdot \mathbf{S}_{l+2} - h \sum_l S_l^z, \quad (1)$$

with the NN exchange  $J_1 < 0$ , the NNN interaction  $J_2 > 0$ , and  $h$  as the external magnetic field along the  $z$  direction. For these materials, it has been shown that the ground state of the 1D Hamiltonian (1) has an instability towards field-induced multipolar Tomonaga-Luttinger-liquid phases,<sup>11-18</sup> and which is interpreted as a hard-core Bose gas of multimagnon bound states undergoing Bose-Einstein condensation at fields slightly lower than the saturation field,  $H_s$ . The ground state of the 1D Hamiltonian (1) is ferromagnetically ordered for  $\alpha = |J_2/J_1| < 0.25$ . At  $|J_2/J_1| = 0.25$ , the FM state is degenerated with a singlet state, while for  $|J_2/J_1| > 0.25$  the ground state is an incommensurate singlet. For a corresponding quasi-1D system with small but finite interchain couplings, the latter situation might possibly result in a helical magnetic structure with an acute pitch (screw) angle. However, depending on the strength of the exchange anisotropy and/or the spin-phonon coupling, other types of helicoidal magnetically ordered states can be realized, such as helical structures with obtuse pitch

angles or cycloidal helices, ordinary Néel states, a spin-Peierls phase, or various other massive phases.<sup>19</sup> Despite its initially simplistic appearance, we would like to stress that the  $J_1$ - $J_2$  model under consideration has not yet been fully investigated theoretically, especially with respect to measurable physical quantities. (To illustrate this point see e.g. Refs. [20,21] and references therein.)

The list of materials, which have been thought to be described well by Eq. (1) and which could serve as a testing ground, includes several quasi-one-dimensional (Q1D) edge-sharing chain cuprates, such as  $\text{Rb}_2\text{Cu}_2\text{Mo}_3\text{O}_{12}$ ,  $\text{LiCuVO}_4$ ,  $\text{NaCu}_2\text{O}_2$ ,  $\text{LiCu}_2\text{O}_2$ , and  $\text{PbCuSO}_4(\text{OH})_2$ .<sup>10,22–33</sup> For most of these systems the magnetic couplings – and thus  $H_s$  – are rather large provided the system is not in the vicinity of a ferromagnetic critical point such as  $\text{Li}_2\text{ZrCuO}_4$ . In the latter case, single crystals are still not available making it generally difficult to study effects close to  $H_s$  experimentally using stationary fields.<sup>34–37</sup>

Possibly, only one of these materials, the natural mineral linarite,  $\text{PbCuSO}_4(\text{OH})_2$ , reflects an optimum compromise of a comparatively low  $\alpha$ -value not far from the critical point, *viz.*, a low saturation field, and the availability of single crystals. Despite this, linarite has only been studied superficially to date. According to these initial studies, it has been proposed to represent a frustrated quasi-1D  $J_1 - J_2$  model magnet described by Eq. (1). Linarite crystallizes in a monoclinic lattice (space group  $P2_1/m$ ;  $a = 9.682 \text{ \AA}$ ,  $b = 5.646 \text{ \AA}$ ,  $c = 4.683 \text{ \AA}$ ,  $\beta = 102.66^\circ$ ),<sup>38</sup> in which  $\text{CuO}_2$  units are aligned in chain-like structures along the  $b$  direction (Fig. 1). Each of the  $\text{Cu}^{2+}$  atoms is fourfold coordinated, with the surrounding oxygens forming a flat tetragon close to a square, the celebrated  $\text{CuO}_4$  “plaquette-” “brick” of all undoped cuprates. This is supplemented by four hydrogen atoms as ligands to these planar oxygens. The Cu coordination is completed by two further oxygen atoms from the  $\text{SO}_4$  groups, yielding a distorted octahedron and a slightly non-planar “waving” (buckled)  $\text{CuO}_2$ -chain structure. This is in contrast to the much better studied planar counterpart of the edge-shared chain cuprates  $\text{LiCu}_2\text{O}_2$  and  $\text{LiVCuO}_4$ .

Initial susceptibility and zero-field specific heat data have been interpreted in terms of a dominant magnetic coupling along the chain, with a *predominant* FM-NN interaction  $J_1 = -30 \text{ K}$  and a weaker AFM-NNN coupling  $J_2 = 15 \text{ K}$  ( $\alpha = 0.5$ ).<sup>33</sup> This way, a strong coupling scenario in terms of interacting and interpenetrating simple AFM Heisenberg chains would be envisaged for the  $J_1$ - $J_2$  model under consideration. However, more recent studies by Yasui et al.<sup>22</sup> indicate a rather different *weak*-coupling regime, namely:  $J_1 = (-13 \pm 3) \text{ K}$  and  $J_2 = (21 \pm 5) \text{ K}$  ( $\alpha = 1.6$ ), which have been obtained from a fit to the susceptibility data using a high-temperature expansion up to the fourth-order in the temperature range  $50 < T < 350 \text{ K}$ . Such a weak-coupling regime should give rise to more pronounced frustration and fluctuation effects.<sup>39</sup> The observation of a magnetically ordered state below  $T_N \approx 2.8 \text{ K}$  has been discussed in terms of a possi-

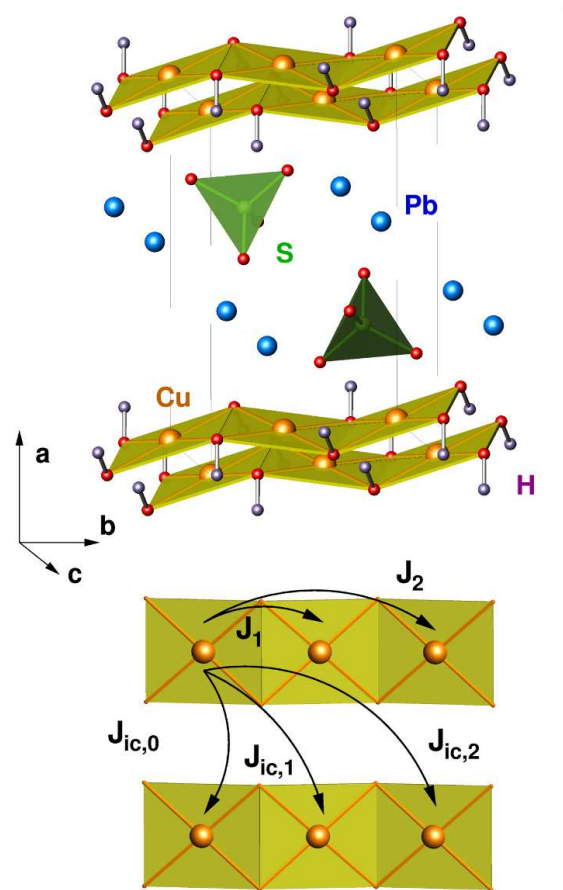


FIG. 1: (Color online) The crystallographic structure and the main exchange paths in  $\text{PbCuSO}_4(\text{OH})_2$ . The  $\text{CuO}_2$  units are aligned in the  $bc$  plane, forming edge-sharing  $\text{CuO}_2$  chains along the  $b$  direction. In order to illustrate the coordination of the S atoms, oxygen tetrahedra are highlighted in the sketch. The two inequivalent alternating “left” and “right” proton positions distinguished by bond lengths and bond angles are according to Ref. 38.

ble helical ground state with an acute pitch angle.<sup>33</sup> The helical nature of the ground state is supported by a recent study of the dielectric constant in this material.<sup>22</sup> However, microscopic studies such as NMR or neutron scattering measurements to prove these predictions are still lacking. Although in both references a similar conclusion has been obtained regarding the basic nature of the magnetic ground state of linarite,<sup>22,33</sup> the physical characteristics of the spiral and thus the magnetic properties would differ enormously due to e.g. the relevance of quantum effects on the pitch angle and on the magnetic moment in the ordered state.

In view of these conflicting results, we started a detailed study on this material combining macroscopic and microscopic experimental techniques with different theoretical methods to resolve the magnetic exchange parameters of  $\text{PbCuSO}_4(\text{OH})_2$  and, thus, its underlying ground state. Measurements of the static susceptibility and the

saturation magnetization have been performed. The intrinsic spin susceptibility is investigated utilizing ESR and NMR. Measurements of the  $g$ -factor as well as of the ESR and NMR linewidths indicate an appreciable magnetic anisotropy in our system and further emphasize the highly frustrated character of linarite with an onset of magnetic correlations far above the magnetic ordering temperature. An analysis of our data within advanced theoretical methods, such as density matrix renormalization group (DMRG), hard-core boson technique and local (spin-polarized) density approximation (L(S)DA+ $U$ ) calculations, which all take into account the nontrivial interplay of quantum effects and frustration beyond linear spin-wave theory, yield new values for the exchange couplings along the chain directions of  $J_1 \sim -100$  K and  $J_2 \sim 36$  K. These values are substantially larger than those determined previously.<sup>22,33</sup> Within our extensive analysis, we succeeded in estimating the order of magnitude of the interchain couplings. The theoretical part of the present paper should be understood also as a step in the direction to fill the existing gap of the not fully explored  $J_1 - J_2$  model, beyond providing an assignment of the main exchange parameters for a specific material only. In particular, a precise knowledge of the main exchange parameters is one of the prerequisites to attack in a realistic manner rather complex and not yet fully understood phenomena such as multiferroicity<sup>22</sup> and multipolar phases/spin nematics<sup>12</sup> reported or suggested for the title compound, too.

## II. METHODS

### A. Experimental

#### 1. Samples and diffractions

The single crystals of  $\text{PbCuSO}_4(\text{OH})_2$  used in this study for the magnetization, NMR, and X-band ESR measurements are natural minerals with their origin in California, USA (*origin 1*: Blue Bell Mine, Baker, San Bernadino). A second set of naturally grown single crystals of smaller size (*origin 2*: Siegerland, Germany) has been used for the ESR measurements in a resonant cavity at a frequency of about 93 GHz. All crystals show well-defined facets and the principal axes  $b$  and  $c$  can be identified easily. Single crystallinity of our samples has been checked by x-ray diffraction. For both sets of single crystals no magnetic impurity phases were observed within experimental resolution, as evidenced by the absence of a low-temperature Curie tail in the magnetic susceptibility. For all measurements the samples were oriented along the principle crystallographic directions with a possible misalignment of less than  $5^\circ$ .

#### 2. Magnetization

Temperature-dependent magnetization studies of linarite were performed using a commercial SQUID magnetometer in the temperature range 1.8 - 400 K and in an external magnetic field of 0.4 T. Magnetization curves,  $M(H)$ , were measured at  $T = 1.8$  and 2.8 K in a commercial Physical Properties Measurement System using a Vibrating Sample Magnetometer (VSM). Magnetization data were collected while sweeping the magnetic field using sweep rates of about 50 Oe/s for both increasing and decreasing field regimes. Note that due to hysteresis around the phase transitions observed for the 1.8 K data, the sweep rate was significantly varied in these regions in order to check for sweep-rate dependent effects on the phase transitions. Using quasi-static conditions, the observed small hysteresis in the  $M(H)$  curves became negligible, as shown below.

#### 3. Electron Spin Resonance (ESR)

For the ESR experiments two different setups were used. The commercial X-band spectrometer operates at a frequency of about 9.6 GHz. This allows sweeps of the magnetic field up to 1 T. The setup is equipped with a continuous-flow liquid-helium cryostat, enabling measurements from room temperature down to about 4 K. The cryostat is inserted in a rectangular microwave resonator in the TE102 mode configuration. Samples are mounted on a quartz sample holder, which is centered in the resonator at the maximum of the microwave magnetic field. The sample holder can be rotated with respect to the external magnetic field. By using an additional external magnetic modulation field, the lock-in detection technique is applied. The second setup consists of a microwave vector network analyzer (MVNA) and a 15 Tesla superconducting magnet.<sup>40</sup> This setup allows phase-sensitive measurements at different frequencies in the range from 30-800 GHz. Most experiments were carried out using a home-built cylindrical resonator in the TE011 configuration with a resonance frequency of about 93 GHz. For this, the samples were mounted on a quartz needle in the center of the resonator. The resonator is coupled to a metallic waveguide, which is placed in the center of the superconducting magnet. The very high quality factor of the order of  $Q \sim 10^4$  – and, thus, the high sensitivity of this resonator setup – allowed the measurement of single crystals of linarite with dimensions of approximately  $0.5 \times 0.5 \times 1 \text{ mm}^3$  with very high signal-to-noise ratio.

#### 4. Nuclear Magnetic Resonance (NMR)

$^1\text{H}$ -NMR ( $^1\gamma = 42.5749 \text{ MHz/T}$ ) and  $^{207}\text{Pb}$ -NMR ( $^{207}\gamma = 8.9074 \text{ MHz/T}$ ) measurements were performed

using a phase-coherent Tecmag spectrometer with a He-flow cryostat for temperatures down to 4.2 K and magnetic fields of 2 and 4 T, respectively. Temperatures below 4.2 K were achieved by pumping on the helium bath. The NMR spectra were determined using a  $\pi/2 - \tau - \pi$  Hahn spin-echo pulse sequence. Special care was taken to avoid extrinsic signals from parasitic  $^1\text{H}$  atoms around the sample. Due to the strong increase of the linewidth at low temperatures, additional field sweeps at constant frequency have been performed. This way, we can ensure that neither the selected frequency excitation spectrum by the pulse width (typically a  $\pi/2$ -pulse is about 3  $\mu\text{s}$ ) nor the quality factor of our coil do artificially narrow the detected lines of  $\text{PbCuSO}_4(\text{OH})_2$ . The spin-lattice relaxation time  $T_1$  has been recorded using an inversion-recovery pulse sequence ( $\pi - \tau_{\text{var}} - \pi/2 - \tau - \pi$ ) with variable delay  $\tau_{\text{var}}$  and a Hahn spin-echo detection at the end. Typical conditions of excitation were 3  $\mu\text{s}$  and 6  $\mu\text{s}$  for a  $\pi/2$ - and  $\pi$ -pulse, respectively. Repetition rates were in the range 100 - 400 ms despite short spin-lattice relaxation times  $T_1$  in order to avoid any local heating at the sample site. For  $H \parallel b$ , the spin-lattice relaxation rate of the  $^1\text{H}$  nucleus was determined using a saturation-recovery sequence with an echo subsequence at the end, i.e.,  $(\pi/2 - \tau_{\text{del}})_n - \tau_{\text{var}} - \pi/2 - \tau - \pi$  with the delay time  $\tau_{\text{del}}$  and  $n$  as the number of repetitions of the first cycle. Calibration of the fields has been performed using the  $^1\text{H}$ - and  $^2\text{D}$ -NMR resonance frequencies of hydrogenated and deuterated water at room temperature for the 2 and 4 T experiments, respectively.

## B. Theoretical methods

### 1. DMRG and TMRG

Initially, we analyzed the saturation field using well-known rigorous expressions valid in the so-called two-magnon and one-magnon sectors depending on the strength of the interchain coupling. Next, we considered the magnetization curve at low  $T$ , say 1.8 K, for  $H \perp (bc)$  and compared our calculations with the experimental data shown in Fig. 3 for this direction. To calculate the magnetic susceptibility we employed the transfer-matrix renormalization group (TMRG) method.<sup>41-43</sup> In our calculations, 80-160 states were retained in the renormalization procedure and the truncation error was less than  $10^{-4}$  down to  $T = 0.003|J_1|$ .

To calculate the static spin-structure factor  $S(q) = (1/L^2) \sum_{i,j=1}^L [\langle S_i^z S_j^z \rangle - \langle S_i^z \rangle \langle S_j^z \rangle]$ , where  $S_i^z$  denotes the  $z$ -component of the spin at site  $i$ , we used the density-matrix renormalization group (DMRG) method.<sup>44</sup> We studied single chains (two coupled chains) with length up to  $L = 512$  ( $L = 96$ ) and keeping up to  $m = 4000$  ( $m = 2000$ ) density-matrix eigenstates in the renormalization procedure such that the truncation error was less than  $10^{-9}$  ( $10^{-6}$ ). In the single-chain case, the calculated values were extrapolated to the thermodynamic

limit  $L \rightarrow \infty$ . We calculated the magnetization curve at very low temperature ( $T/J \ll 1$ ) using the DMRG technique. The magnetization for a given magnetic field was obtained as

$$M = \frac{\sum_{n=0}^{m_c} \langle \psi_n | S_z | \psi_n \rangle \exp(-\frac{E_n}{k_B T})}{\sum_{n=0}^{m_c} \exp(-\frac{E_n}{k_B T})}, \quad (2)$$

where  $E_n$  and  $\psi_n$  are the  $n$ -th eigenenergy and the eigenstate ( $n = 0$  denotes the ground state), respectively,  $k_B$  is the Boltzmann constant, and  $m_c$  is a cutoff number of the excited-state energies. The cutoff number  $m_c$  desirably should be sufficiently smaller than the number of states  $m$  kept in the density-matrix renormalization step. In this paper, for a fixed system length  $L = 64$  and temperature  $T = 1.8$  K,  $m_c$  varied from 40 to 100 while keeping  $m = 1000$  and  $M$  was extrapolated to the large  $m_c$  limit.

Applying the TMRG technique we analyzed the magnetic spin susceptibility,  $\chi(T)$ , to obtain its maximum position,  $T_\chi^{\text{max}}$ , as a function of the frustration parameter  $\alpha$ . Notice that in the adopted random phase approximation (RPA) for the interchain coupling (IC)  $T_\chi^{\text{max}}$  of the 3D susceptibility,  $\chi_{3D}(T)$ , is independent of the IC, the  $g$ -factor, and the background susceptibility  $\chi_0$ .

### 2. Local spin density $L(S)\text{DA}+U$ calculations

In the second part, we calculate the total energies for various prepared magnetic states, i.e., a ferromagnetic, and various antiferromagnetic states, whose total energy differences were mapped onto those of corresponding spin states of a generalized  $J_1$ - $J_2$  model with supplemented interchain interactions. This way, the main exchange integrals could be extracted.<sup>36,45</sup> The density functional theory (DFT) based electronic-structure calculations were performed using the full potential local orbital scheme FPLO9.00-33.<sup>46,47</sup> Within the scalar relativistic calculation the exchange and correlation potential of Perdew and Wang was applied.<sup>48</sup> For the LSDA+ $U$  calculations we varied  $U$  in the physical relevant range from 5 to 8 eV using the mean-field approximation of the double-counting correction. To ensure convergency we considered 518  $k$  points within the irreducible part of the Brillouin zone.

## III. MAGNETIC SUSCEPTIBILITY

Figure 2 displays the temperature dependence of the macroscopic susceptibility  $\chi(T)$  of linarite with the magnetic field applied along the three principle crystallographic directions. The susceptibility exhibits two characteristic features in the low-temperature region, i.e., a maximum around  $T_\chi^{\text{max}} = 4.9 \pm 0.3$  K (averaged over all three crystallographic directions, see below), just above



the Néel temperature  $T_N$  visible as a pronounced kink around 2.8 K. While the maximum around 5 K is very common in quasi-1D frustrated "ferromagnets" in the vicinity of the critical ferromagnetic-helical point<sup>34</sup> (see also Fig. 13 in Sect. VI) and is associated to low-lying ferromagnetic excitations, the kink at lower temperatures is related to the transition into a long-range magnetically ordered state. From the derivative  $d(\chi T)/dT$  of the susceptibility data (insets in Fig. 2) the transition temperature  $T_N = 2.75(5)$  K is determined.

While the qualitative behavior of  $\chi(T)$  with respect to the three crystallographic directions is the same, the absolute values of  $\chi_{max}$  at  $T_{\chi}^{max}$  differ slightly with  $T_{\chi}^{max} = 5.0 \pm 0.2$  K for  $H \parallel a$ ,  $T_{\chi}^{max} = 4.6 \pm 0.3$  K for  $H \parallel b$ , and  $T_{\chi}^{max} = 4.9 \pm 0.2$  K for  $H \parallel c$ . From this observation, one already might speculate that the  $b$ -axis should be the easy axis, despite of the larger error bars of  $T_{\chi}^{max}$ . We would like to stress, that our  $T_{\chi}^{max}$  values are in agreement with those reported in Ref. 33, while they differ from those of Yasui et al.,<sup>22</sup> where  $T_{\chi}^{max}$  lies between 3.8 - 5 K and becomes maximal for  $H \parallel a'$ . The origin of this discrepancy is not clear up to now, although one possible scenario could be related to small impurity contributions yielding an additional Curie-like contribution, this way shifting  $T_{\chi}^{max}$  to lower temperatures.

In Fig. 3, we present the magnetization data  $M(\mu_0 H)$  and the derivatives  $dM/d(\mu_0 H)$  of  $\text{PbCuSO}_4(\text{OH})_2$  as a function of field at  $T = 1.8$  K  $< T_N$  and  $T = 2.8$  K  $\geq T_N$  with  $H \perp$  (bc) (hereafter named  $a_{\perp}$ ),  $H \parallel b$ , and  $H \parallel c$ .<sup>49</sup> Although here we will focus on the properties of linarite in the paramagnetic regime, we added the low-temperature data in order to extract the saturation field,  $H_s$ , in the case of reduced thermal fluctuations. Measurements were made for increasing and decreasing field; no hysteresis has been observed within the experimental resolution as result of a low sweep rate. Comparing the magnetization versus field (and its derivative), a large anisotropic response is observed with  $M_{s,a_{\perp}} \approx 1.16 \mu_B/\text{Cu atom}$ ,  $M_{s,b} \approx 1.05 \mu_B/\text{Cu atom}$ , and  $M_{s,c} \approx 1.15 \mu_B/\text{Cu atom}$  for the  $a_{\perp}$ ,  $b$ , and  $c$  direction, respectively. Together with the anisotropic values of the saturation field  $\mu_0 H_s$ , i.e.,  $\mu_0 H_{s,a_{\perp}} \approx 7.6$  T,  $\mu_0 H_{s,b} \approx 10.5$  T, and  $\mu_0 H_{s,c} \approx 8.5$  T, this implies an appreciable anisotropy of the magnetic exchange in our compound.

The anisotropic magnetic behavior of  $\text{PbCuSO}_4(\text{OH})_2$  is also evidenced in the number of transitions observed in the  $dM/d(\mu_0 H)$  curve at 1.8 K. While for the  $a_{\perp}$  and  $c$  directions only one sharp peak indicative of a phase transition is observed (around  $\mu_0 H_{c3} \approx 5.2$ -5.5 T), for the  $b$  direction, i.e., for the chain direction, three clear transitions could be resolved at  $\mu_0 H_{c1}^b \approx 2.7$  T,  $\mu_0 H_{c2}^b \approx 3.3$  T, and  $\mu_0 H_{c3}^b \approx 5.8$  T. These transitions at low fields possibly assign rotation and spin-flop reorientations out of a helical ground state for the field aligned along the easy magnetic axis. We will discuss this behavior in more detail in a forthcoming paper.<sup>50</sup>

Both the anisotropy and the overall small saturation field of linarite are very important and unique features

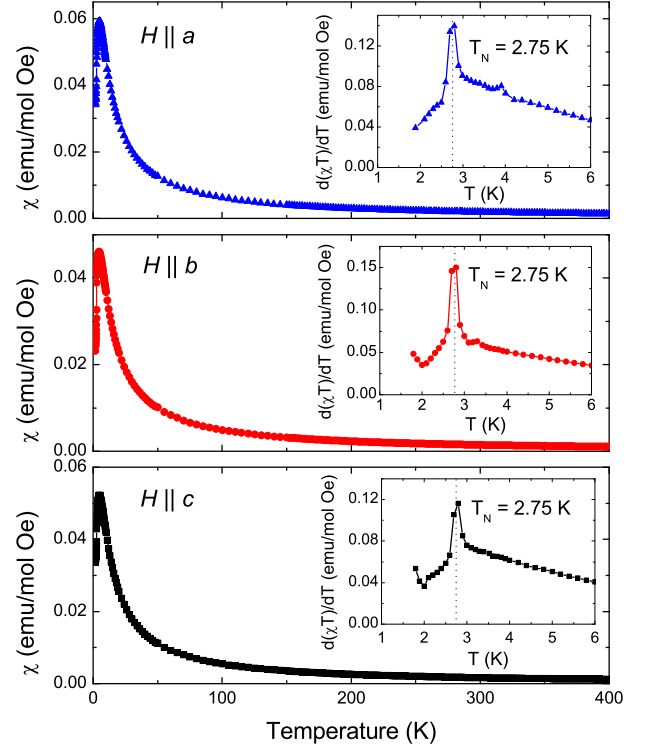


FIG. 2: (Color online) Temperature dependence of the magnetic susceptibility of  $\text{PbCuSO}_4(\text{OH})_2$  for an external magnetic field of 0.4 T applied parallel to the  $a$ ,  $b$ , and  $c$  axes. In the insets, the derivatives  $d(\chi T)/dT$  as function of temperature are shown, from which the magnetic ordering temperature  $T_N \approx 2.75(5)$  K can be evaluated.

with respect to the predicted exotic high-field phases. This makes  $\text{PbCuSO}_4(\text{OH})_2$  suitable for the investigation of such phenomena in easily available static magnetic fields. In order to resolve the origin of the magnetic anisotropy in linarite, which could either stem from  $g$ -factor anisotropy, anisotropic exchange, or antisymmetric Dzyaloshinskii-Moriya interactions to name a few, we performed ESR investigations.

#### IV. ELECTRON SPIN RESONANCE (ESR)

ESR measurements were performed for different single crystals of linarite. A small single crystal from *origin 2* was used for the measurements in the resonant cavity at a frequency of about 93 GHz. At this frequency, the resonance field is found around 3 T. The spectrum consists of a single line of Lorentzian shape (Fig. 4). From a fit to the ESR lines, the intensity, the resonance field, and the linewidth are extracted. From those parameters the integrated ESR intensity, which is determined by the intrinsic spin susceptibility, was calculated (see Fig. 9 and discussion in the following NMR section). Since the resonator was inserted into the cryostat its quality factor  $Q$  and

its resonance frequency  $\nu_{\text{res}}$  change with temperature.  $Q$  and  $\nu_{\text{res}}$  are determined with frequency sweeps around the resonance frequency at every temperature and the spin susceptibility  $\chi_s$  and resonance field  $H_{\text{res}}$  can be corrected accordingly.

The temperature dependencies of the ESR resonance field and ESR linewidth are plotted in Fig. 5.<sup>51</sup> In the high-temperature regime (roughly above 50 K) the resonance fields are temperature independent. A shift of the resonance position of an ESR signal as a function of temperature is associated with the development of internal magnetic fields in the system. Along the  $b$  direction a shift is observed only at low temperatures close to the ordering temperature  $T_N$ . This shows that an internal field develops along the chain direction only when the actual 3D ordering occurs. However, along the  $a$  and  $c$  directions a shift in the resonance field is observed already at much higher temperatures starting at around 50 K and developing smoothly with decreasing temperature. This indicates that the Cu spins are primarily aligned in the  $ac$  plane, but do not point along the chain direction in the paramagnetic regime. The internal fields developing are, therefore, predominantly directed perpendicular to the chain direction. At first glance, the above considerations are in some conflict with the magnetization measurements indicating that the  $b$  axis might be the easy axis of our system. However, taking into account that

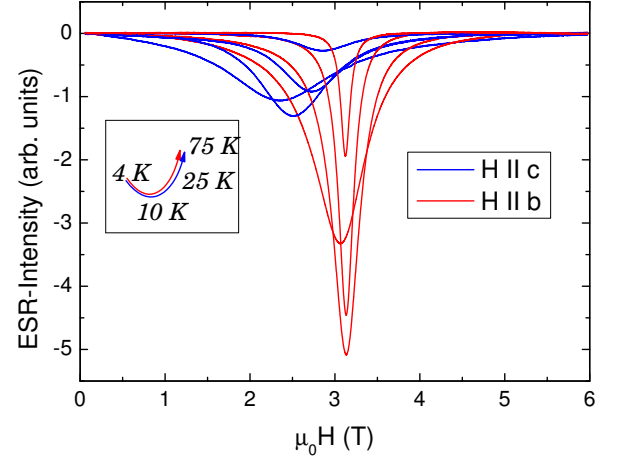


FIG. 4: (Color online) ESR spectra for different temperatures measured at 93 GHz with the magnetic field  $H$  applied along the  $b$  and  $c$  axes. Spectra for  $H \parallel a$  (not shown) are similar to spectra for  $H \parallel c$ . Arrows on the left side indicate temperatures of the individual ESR spectra.

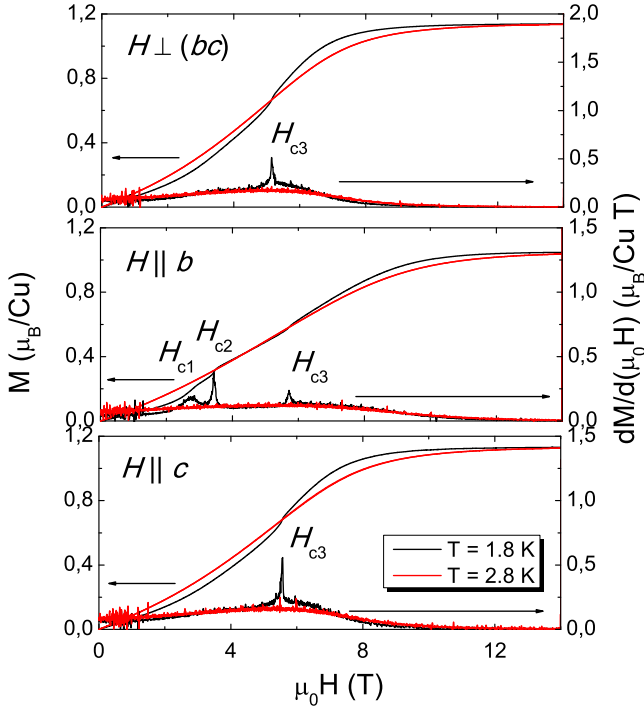


FIG. 3: (Color online) Magnetization curve  $M(\mu_0 H)$  and its derivative  $dM/d(\mu_0 H)$  for magnetic fields applied along  $a_\perp$ ,  $b$ , and  $c$  of  $\text{PbCuSO}_4(\text{OH})_2$  measured at  $T = 1.8 \text{ K} < T_N$  (black curves) and  $T = 2.8 \text{ K} \geq T_N$  (red curves).

the magnetic field used in the ESR measurements ( $\sim 3$  Tesla) will probably be strong enough to rotate the pre-spiral orientation out of the easy-plane (see Sect. III), even at high temperatures above  $T_N$  short-range ordered clusters could explain our observations with predominant internal fields perpendicular to the chain direction.

From the resonance field,  $H_{\text{res}}$ , the effective  $g$ -factors along the crystallographic directions can be determined as  $g = h \cdot \nu_{\text{res}} / (\mu_B H_{\text{res}})$ . For the high-temperature regime the effective  $g$ -factors are found to be  $g_a = 2.34$ ,  $g_b = 2.10$ , and  $g_c = 2.28$ .

Having established the  $g$ -factors for the three principal crystallographic directions, we can analyze the magnetic anisotropy in our system. In Fig. 6, we present the spin expectation value  $\langle S_z \rangle = M / N g \mu_B$  ( $N$ : Avogadro number) of  $\text{PbCuSO}_4(\text{OH})_2$  as a function of the scaled field  $g \mu_0 H$  at 2.8 and 1.8 K and for the three crystallographic directions  $a_\perp$ ,  $b$ , and  $c$  as derived from the experimentally determined magnetization data  $M(H)$  (Fig. 3). The extracted spin expectation value corresponds to the Cu spin 1/2. In the paramagnetic regime above  $T_N$ , the anisotropy of both saturation magnetization and saturation field is explained mainly by the anisotropy of the  $g$ -factor. Note that there is a difference in the calculated and directly measured saturation magnetization for  $H \parallel a_\perp$  due to the  $g$ -factor. For the ESR experiment the magnetic field was aligned along  $a$ , while for the magnetization measurement the field was aligned perpendicular to the  $bc$  plane. For an alignment along  $a$  the saturation magnetization would be slightly larger and would match the calculated value. For temperatures smaller than  $T_N$ , however, the anisotropy cannot be described by the  $g$ -factor anisotropy. Additional contributions from symmetric exchange anisotropy and/or possibly Dzyaloshinskii-Moriya interactions need to be taken

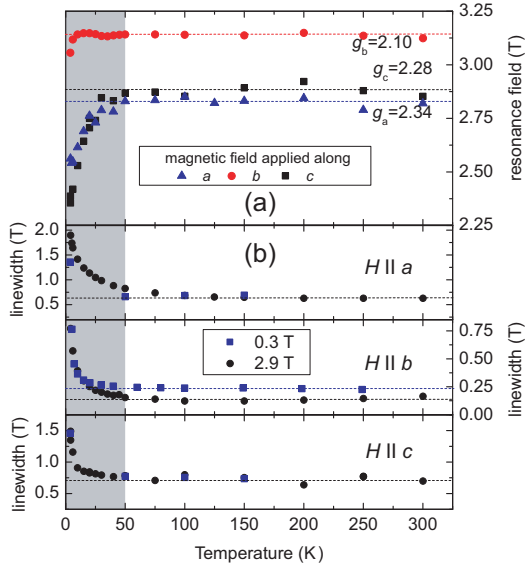


FIG. 5: (Color online) (a) Resonance fields at about 93 GHz and (b) linewidths for resonance fields of about 0.3 and 2.9 T of the ESR signals as a function of temperature for the external magnetic field applied along the crystallographic axes  $a$ ,  $b$ , and  $c$ . The resonance field is temperature independent above  $\sim 50$  K and decreases with decreasing temperature. For the high-temperature resonant fields the corresponding  $g$ -factors are listed. The linewidth is significantly smaller for  $H \parallel b$ .

into account.

As shown in Fig. 5, the ESR linewidth is strongly anisotropic. At a frequency of 93 GHz corresponding to a resonance field of about  $H_{res} \approx 3$  T, the linewidth for  $H \parallel b$  is with  $\Delta H \approx 0.13$  T much smaller than  $\Delta H \approx 0.7$  T for  $H \parallel a$  and  $c$ . For all directions the linewidth is almost constant or only weakly dependent on temperature above 50 K. At the X-band frequency of about 9.6 GHz - corresponding to  $H_{res} \approx 0.3$  T - the temperature dependencies of the ESR signals show a similar behavior (squares in Fig. 5(b)). The linewidths along  $a$  and  $c$  are - within the uncertainty of the measurement - identical to the linewidths at higher fields. The decreasing intensity of the ESR signal with increasing temperature makes it difficult to analyze the lines perfectly along those orientations up to room temperature, however, the linewidth appears to stay constant. For the  $b$  direction at high temperatures, the linewidth is constant and fairly narrow with  $\Delta H \approx 0.25$  T, which is unexpected since it is broader than for the larger field of about 3 T. This effect can be explained by the strongly anisotropic linewidth together with a slight misalignment of the sample of about  $5^\circ$  for this particular measurement.

On approaching temperatures below 50 K a broadening of the lines is observed for both fields. The small resonance field of about 0.3 T limits the reliability of the measurements for fields aligned along  $a$  and  $c$ , since the linewidth exceeds the resonance field and a fit to the data

cannot be done accurately anymore. However, the values are close to the linewidths for the ten times larger field of about 3 T.

The ESR linewidth depends on (dipolar) spin-spin or anisotropic exchange interactions as well as on the development of internal magnetic fields. The fact that the linewidth is the same for different fields indicates that inhomogeneous broadening effects are rather small. As we approach lower temperatures the spin-spin correlation length increases and short-range magnetic correlations develop. The change of linewidth as a function of temperature yields information about the dimensionality and type of interactions in the system. The broadening can be analyzed in terms of

$$\Delta H(T) = \Delta H_0 + C[(T - T_N)/T_N]^{-p} \quad (3)$$

as the ordering temperature is approached. The linewidth,  $\Delta H(T)$ , is divided into a non-critical constant part,  $\Delta H_0$ , and a temperature-dependent critical part,  $\Delta H_{crit}(T)$ .<sup>52</sup> The exponent  $p$  yields information about the effective dimensionality of the correlated spin system and its change by approaching a long-range-ordered ground state. Fits to our data over the low-temperature range with a fixed  $T_N = 2.0$  K at 3 T result in critical exponents  $p = 0.5$ - $0.8$  (Fig. 7). Note, that the magnetic

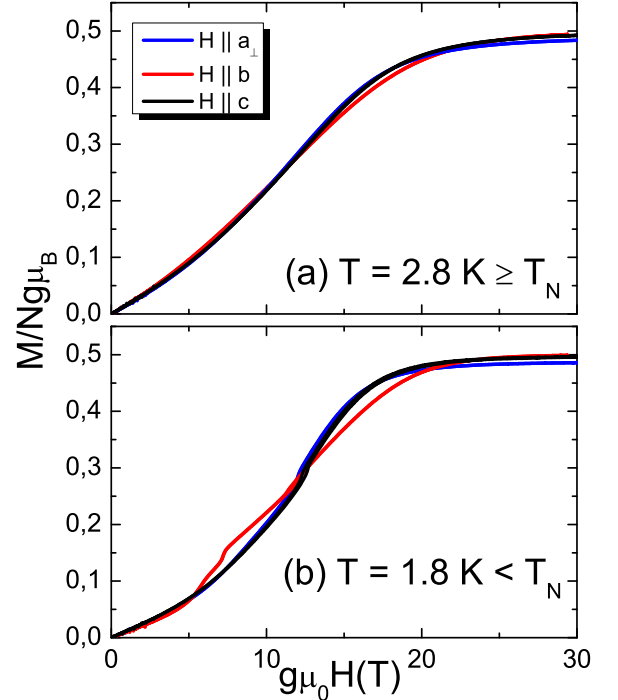


FIG. 6: (Color online) The experimentally determined spin expectation value  $\langle S_z \rangle = M/Ng\mu_B$  of  $\text{PbCuSO}_4(\text{OH})_2$  as a function of the scaled magnetic field  $g\mu_0 H$  along different crystallographic directions and temperatures (a)  $T = 2.8$  K  $\geq T_N$  and (b)  $T = 1.8$  K  $< T_N$ .

ordering temperature  $T_N = 2.0$  K was chosen according to the field dependence of  $T_N$  as determined by thermodynamic bulk measurements.<sup>50</sup> For a 1D Heisenberg magnet the critical exponent was found to be about  $p = 2.5$ .<sup>53</sup> However, on approaching the ordering temperature this value can change significantly and values of  $p \approx 0.6$  have been reported.<sup>52</sup> Such a critical exponent is interpreted as signalling the appearance of 3D antiferromagnetic fluctuations. The fact that the broadening in our system occurs already at temperatures around 50 K, *i.e.*, 15 times higher than the actual ordering temperature, points to appreciable magnetic fluctuations at elevated temperatures indicative of substantial interlayer correlations well above  $T_N$ . The actual 3D ordering at much lower temperatures then indicates a strongly frustrated system with competing interactions on the energy scale of  $\sim 50$  K.

## V. NUCLEAR MAGNETIC RESONANCE (NMR)

Our NMR experiments were conducted using  $^1\text{H}$ - and  $^{207}\text{Pb}$  as probing nuclei. Both the hydrogen and the lead ions occupy low-symmetric crystallographic sites with respect to the magnetic Cu sites, *i.e.*, none of the ions are located exactly between two Cu ions neither along the chain nor between two neighboring chain structures. While there is only one crystallographic site for Pb, two inequivalent H sites can be expected according to recent structural investigations via neutron diffraction emphasizing two different kinds of hydrogen bondings in linarite.<sup>38</sup> Henceforth, a single  $^{207}\text{Pb}$  and two  $^1\text{H}$ -NMR lines can generally be expected in our experiment. We name

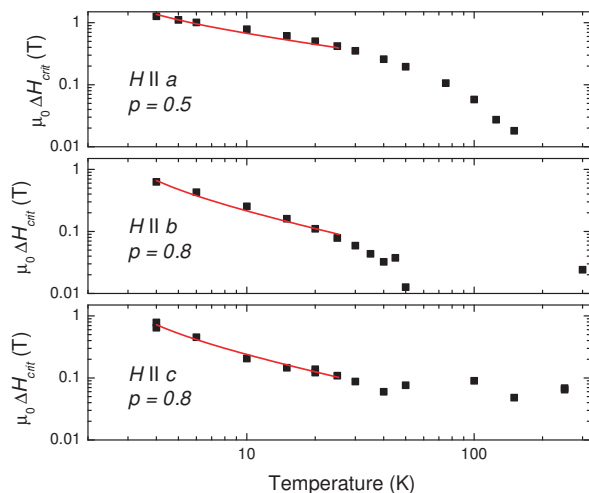


FIG. 7: (Color online) Double logarithmic plot of the critical linewidth part  $\Delta H_{crit}$  (from ESR) as a function of temperature for  $H$  parallel to the three crystallographic directions  $a$ ,  $b$ , and  $c$ . Fits to the data for temperatures up to 25 K are shown.

the hydrogen site with the stronger bonding  $H_1$ , *i.e.*, probably the one with the larger hyperfine coupling, and the one with the weaker bonding  $H_2$ . For magnetic fields  $H \parallel b$ , however, two nearly overlapping  $^1\text{H}$  resonance lines imply that both hyperfine couplings are nearly identical for this field direction. We have also tried to detect the  $^{63,65}\text{Cu}$  spin-echo signals, but did not succeed. We attribute the lack of copper signal to very short spin-spin relaxation times  $T_2$  of linarite, which are of the order of 20  $\mu\text{s}$  at room temperature even at the  $^{207}\text{Pb}$  and  $^1\text{H}$  sites.

The interest in probing both  $^1\text{H}$  and  $^{207}\text{Pb}$  lies in the different coupling of the two nuclei with their neighboring atoms and thus different distances and symmetries with respect to the magnetic  $\text{Cu}^{2+}$  ions. From the crystallographic structure and chemical-bonding scheme it can be expected that due to the distance between Pb and neighboring magnetic Cu ions the hyperfine coupling at the  $^{207}\text{Pb}$  site will be dominated by dipolar couplings between Pb nuclei and Cu spins. At the  $^{207}\text{Pb}$  site, the dipolar fields will be predominantly given by the spins of the two nearest magnetic ions, *i.e.*, two Cu spins along the chain ( $b$ ) direction. But also couplings to next-nearest neighboring Cu ions along the chain as well as neighboring chains along  $c$  and  $a$  can be expected to result in small additional contributions. On the other hand, at the  $^1\text{H}$  site, the effective local fields at the probing nuclei are probably composed of the dipole fields of surrounding magnetic  $\text{Cu}^{2+}$  moments and of so-called contact fields. The latter are due to the direct neighboring environment of hydrogen and oxygen atoms, which mediate the magnetic superexchange between magnetic Cu ions. In this situation a small polarization of the hydrogen atoms can be envisaged. Since the hydrogen atoms are located very close to the  $bc$  plane of  $\text{Cu}^{2+}$  ions, the hyperfine fields will be predominantly given by the spins of the four nearest magnetic ions of the nearest neighboring  $bc$  plane, *i.e.*, two neighboring Cu spins from one and two neighboring Cu spins from a second Cu-chain shifted by the lattice constant  $c$ .

The spin-echo signal of the  $^1\text{H}$  and  $^{207}\text{Pb}$  lines was observed in the temperature range 5 - 400 K. We first analyze the resonance shift of the  $^1\text{H}$  and  $^{207}\text{Pb}$ -NMR lines for an applied magnetic field of 2 and 4 T, respectively (Fig. 8). The different field values have been used in order to obtain reasonable frequency ranges for both nuclei. Due to strong transverse magnetic short-range correlations leading to a very short spin-spin relaxation time  $T_2$  of less than 5  $\mu\text{s}$  at low temperatures, a wipe-out of the  $^{207}\text{Pb}$ -NMR signal occurs below  $\sim 10$  K. The NMR shift is defined as the normalized difference between the observed resonance frequency,  $\omega_{res}$ , and the calculated value for the bare nucleus,

$$K(T) = \frac{\omega_{res} - \gamma\mu_0 H_0}{\gamma\mu_0 H_0}, \quad (4)$$

$\gamma$  being the gyromagnetic ratio of the nucleus and  $H_0$



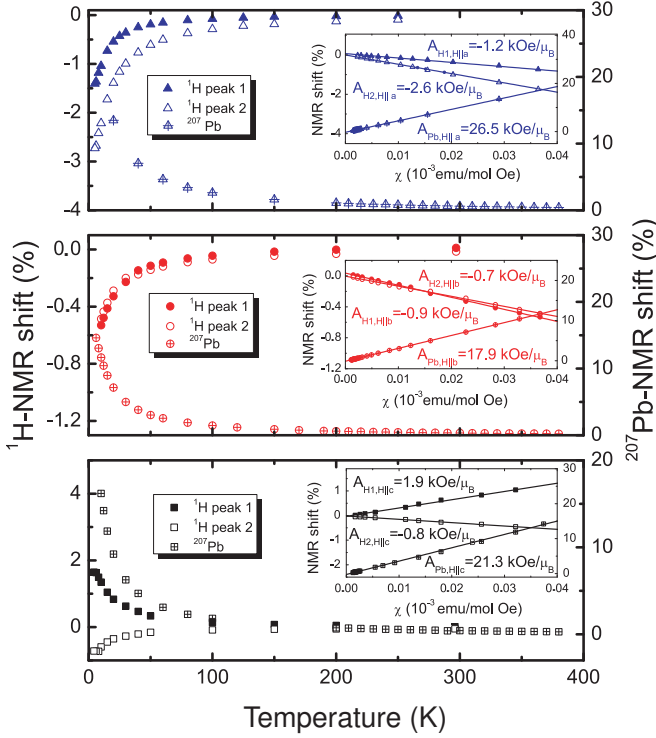


FIG. 8: (Color online) The  $^1\text{H}$ - and  $^{207}\text{Pb}$ -NMR shift of  $\text{PbCuSO}_4(\text{OH})_2$  in the temperature range 5 - 400 K for all three crystallographic directions. While the  $^1\text{H}$  data have been determined in an external field of 2 T, the  $^{207}\text{Pb}$ -NMR shift has been measured in an applied field of 4 T. In the insets, the NMR shifts are plotted as function of the macroscopic bulk susceptibility. The lines represent linear fits to the experimental data; for details see text.

being determined from the  $^1\text{H}$  and  $^2\text{D}$ -NMR resonance frequency of (deuterated) water at room temperature. From Fig. 8 a strong paramagnetic increase of both the  $^1\text{H}$ - and  $^{207}\text{Pb}$ -NMR shift is observed with decreasing temperature, which arises from the interactions between the probing nuclei and the surrounding electrons.

Generally, the NMR shift  $K_{\text{tot}}(T)$  can be divided into two contributions,

$$K_{\text{tot}}(T) = K_{\text{spin}}(T) + K_{\text{orb}}, \quad (5)$$

where  $K_{\text{spin}}(T) = A\chi_{\text{spin}}(T)$  arises via a hyperfine coupling to the electronic spins and  $K_{\text{orb}}$  stems from a temperature-independent orbital magnetization induced at the nucleus site. Here,  $A$  is the hyperfine coupling constant, which can either have a positive or negative sign, leading to positive or negative temperature dependencies of the NMR shift. From this equation it is already obvious that NMR has an advantage over bulk susceptibility investigations. Via NMR one accurately measures the intrinsic spin susceptibility,  $\chi_{\text{spin}}(T)$ , without suffering from temperature-independent diamagnetic core or Van Vleck contributions, from free spins (impurities) and ex-

trinsic foreign phases, which limits the accuracy of bulk susceptibility measurements. Therefore, it is more reliable to extract the magnetic parameters from the temperature dependence of the NMR shift rather than from bulk susceptibility. The conventional scheme of correlating the NMR shift  $K_{\text{tot}}(T)$  and the bulk susceptibility  $\chi(T)$  is to plot both parameters as  $K_{\text{tot}}(\chi)$  with temperature being an implicit parameter. This way, the slope yields the hyperfine coupling constant  $A$ , while  $K_{\text{orb}}$  results from the intersect at  $\chi = 0$ .

The NMR shift as function of the bulk susceptibility of linarite is shown in the insets of Fig. 8 for both nuclei and for the magnetic field applied along the three crystallographic directions. Clearly, both physical properties scale with each other for all cases in the full temperature regime. A linear fit to this data yields highly anisotropic hyperfine coupling constants for both  $^1\text{H}$ -nuclei, *i.e.*,  $A_{H1,H||a} = -1.2 \text{ kOe}/\mu_B$  and  $A_{H2,H||a} = -2.6 \text{ kOe}/\mu_B$ ,  $A_{H1,H||b} = -0.9 \text{ kOe}/\mu_B$ ,  $A_{H2,H||b} = -0.7 \text{ kOe}/\mu_B$ ,  $A_{H1,H||c} = 1.9 \text{ kOe}/\mu_B$  and  $A_{H2,H||c} = -0.8 \text{ kOe}/\mu_B$ . The different hyperfine couplings of the two inequivalent H atoms strongly support the notion of different hydrogen bondings to neighboring oxygen sites in linarite as determined previously.<sup>38</sup> In contrast to these anisotropic values for the  $^1\text{H}$ -nuclei, the  $^{207}\text{Pb}$  hyperfine couplings are dominated by a large positive isotropic contribution, which is complemented by a small anisotropic (dipolar) component for the three different axes, yielding overall large and positive values of  $A_{Pb,H||a} = 26.5 \text{ kOe}/\mu_B$ ,  $A_{Pb,H||b} = 17.9 \text{ kOe}/\mu_B$ , and  $A_{Pb,H||c} = 21.3 \text{ kOe}/\mu_B$  for fields aligned along *a*, *b*, and *c*, respectively.

After having determined the hyperfine couplings for the two different nuclei, the intrinsic spin susceptibility of  $\text{PbCuSO}_4(\text{OH})_2$  can be evaluated via  $\chi_{\text{spin}}(T) = (K_{\text{tot}}(T) - K_{\text{orb}})/A$  for the three crystallographic directions. Fig. 9 depicts these physical properties plotted as the inverse spin susceptibility,  $\chi_{\text{spin}}^{-1}$ , as a function of temperature as derived from the  $^{207}\text{Pb}$ -NMR data.<sup>54</sup> For a comparison we added the spin susceptibility obtained from our ESR investigations after normalizing these data to the value of the static susceptibility at 300 K. From this figure it is clearly visible that the intrinsic spin susceptibility from ESR and NMR scales nicely and is practically identical over the whole temperature range for all crystallographic directions.

Then, from a linear fit of the inverse susceptibility to a Curie-Weiss law  $\chi_{\text{spin}}^{-1}(T) \propto (T - \Theta_{\text{CW}})$  in the *T* region 250 - 400 K, the Curie-Weiss temperature,  $\Theta_{\text{CW}}$ , could be determined for the three directions. Its absolute value is isotropic within the experimental error bars as expected for a  $\text{Cu}^{2+} s = 1/2$  system, yielding  $\Theta_{\text{CW}} = 27(2) \text{ K}$ . The positive value of the Curie-Weiss temperature indicates the predominance of a ferromagnetic coupling. Comparing the Curie-Weiss temperature to the ordering temperature, a ratio  $\Theta_{\text{CW}}/T_N \sim 10$  is extracted for linarite. This quantity is commonly used to judge the level of frustration in a compound, since frustration tends to suppress long-range order. A ratio of 10 shows that frus-

tration is definitely an important issue that needs to be considered in this compound.

In Figs. 10 and 11, the linewidths of the  $^{207}\text{Pb}$ - and the  $^1\text{H}$ -NMR spectra, respectively, are shown as function of temperature for all three crystallographic directions  $a$ ,  $b$ , and  $c$ . In the insets, some  $^{207}\text{Pb}$  and  $^1\text{H}$ -NMR spectra are depicted for applied magnetic fields of 4 and 2 T, respectively, and for 3 different temperatures between 10 and 150 K. In the paramagnetic phase, the spin-echo NMR signal has a rather isotropic Lorentzian lineshape. Since the linewidth at high temperatures is very small, *i.e.*, about 10-25 kHz for all spectra and for all three crystallographic directions, we suggest that our single crystal is of rather high-quality. Note that also for the  $^1\text{H}$ -NMR spectra for  $H \parallel b$  two Lorentzian lines have been used to fit the data since the two NMR lines do not perfectly overlap at low temperatures. In Fig. 11, however, the average of the linewidth of both  $^1\text{H}$ -spectra has been plotted for  $H \parallel b$ .

Similar to the ESR linewidth, the temperature dependence of the full width at half maximum (FWHM) of the NMR spectra is expected to give access to the dynamics of the magnetic correlations and thus to the dynamical critical properties in the paramagnetic regime upon approaching  $T_N$ . The NMR linewidth is related to the spin-spin relaxation time,  $T_2$ , and thus probes the trans-

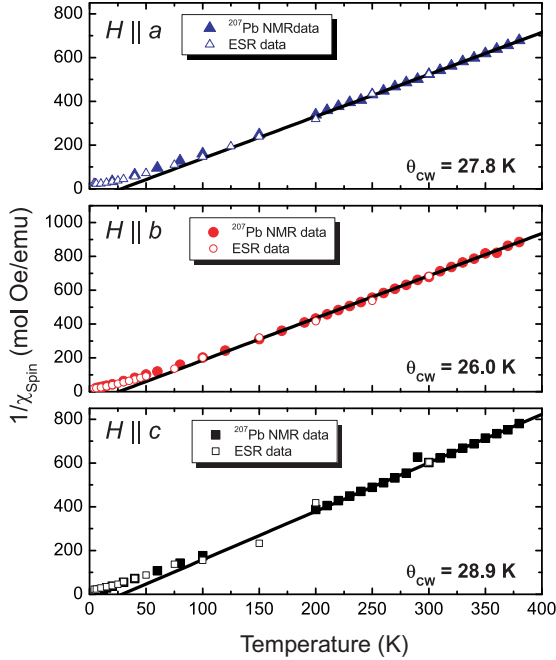


FIG. 9: (Color online) Inverse spin susceptibility of linarite,  $\chi_{\text{spin}}^{-1}(T)$ , for the external magnetic field applied along  $a$ ,  $b$ , and  $c$  as determined via  $^{207}\text{Pb}$ -NMR and ESR. The spin susceptibility as determined via ESR at about 3 T was normalized to the high-temperature (300 K) value of the static susceptibility. The lines represent linear fits to a Curie-Weiss law in the high-temperature range from 250 to 400 K.

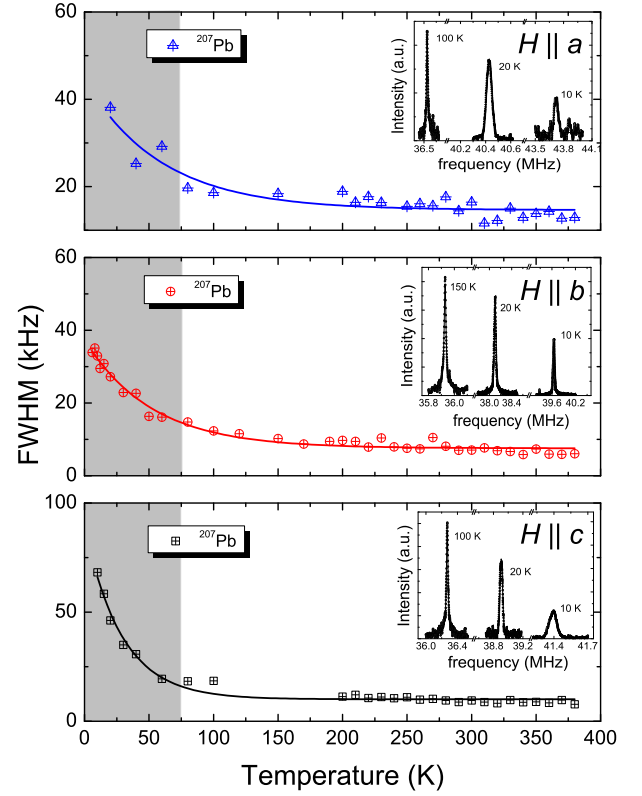


FIG. 10: (Color online) The  $^{207}\text{Pb}$ -NMR linewidth of  $\text{PbCuSO}_4(\text{OH})_2$  as a function of temperature in an external magnetic field of 4 T applied along the three crystallographic axes  $a$ ,  $b$ , and  $c$ . The lines are guides to the eyes. The insets show representative  $^{207}\text{Pb}$ -NMR spectra for different temperatures. The different intensities at these temperatures are not to scale; for details see text.

verse component of the two-spin correlation function and the temporal spin fluctuations of the magnetic system near the critical temperature. Considering a compound with anisotropic magnetic exchange interactions such as linarite, it can be expected that the NMR linewidth is dominated by spin fluctuations along the magnetic easy axis, with spin fluctuations perpendicular to the easy axis only contributing to the non-critical broadening. Hence, taking into account that the linewidth probes transverse spin fluctuations the broadening of the NMR line should be most prominent for magnetic fields perpendicular to this (easy) axis.

For all NMR spectra a pronounced broadening of the line has been observed below  $\sim 75$  K for the  $^{207}\text{Pb}$  signal and below  $\sim 50$  K for the  $^1\text{H}$  spectra. This broadening points to short-range correlations developing already at temperatures  $T \gg T_N$ . Comparing both the response at the two different nuclei and for the three different crystallographic directions, one can easily see that (i) the broadening of the NMR line is shifted to lower temperatures but slightly enhanced for the  $^1\text{H}$  spectra and (ii) that particularly for the 2 T  $^1\text{H}$ -NMR data the broadening is

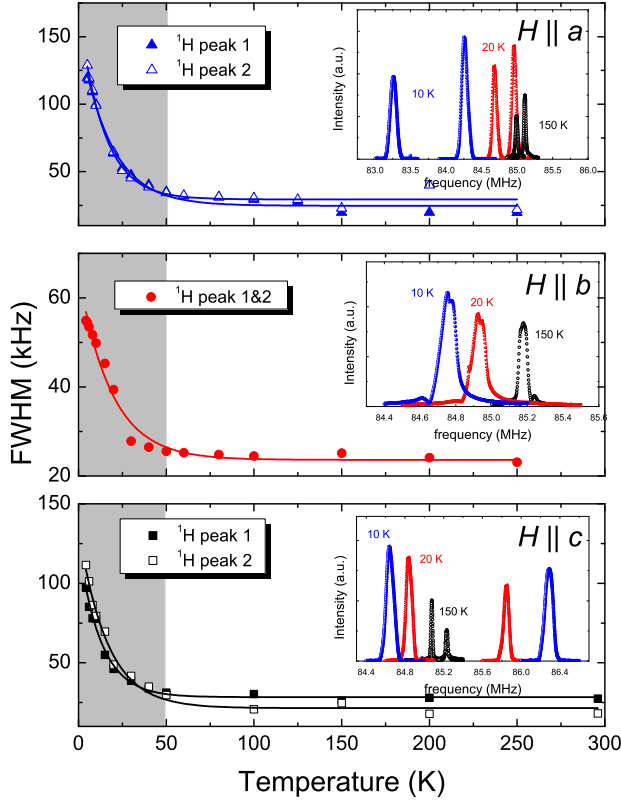


FIG. 11: (Color online) The  $^1\text{H}$ -NMR linewidth of  $\text{PbCuSO}_4(\text{OH})_2$  as function of temperature in an external magnetic field of 2 T parallel to the three crystallographic axes  $a$ ,  $b$ , and  $c$ . The lines represent guides to the eyes. The insets show representative  $^1\text{H}$ -NMR spectra for 10, 20, and 150 K. The intensities at different temperatures are not to scale; for details see text.

more pronounced for the directions perpendicular to the Cu chain. The latter is in perfect agreement with the results obtained from the temperature dependence of the ESR linewidth and emphasizes the magnetic anisotropy in our system.

The temperature dependence of the spin-lattice relaxation rate,  $1/T_1$ , is depicted in Fig. 12 for both probing nuclei and for the external magnetic field parallel to the  $a$ ,  $b$ , and  $c$  axes. Here, we present our spin-lattice relaxation data in both the paramagnetic and the magnetically ordered state below  $T_N$ . This way, a first microscopic proof for the 3D magnetically ordered state is given. Due to the very short spin-spin and also spin-lattice relaxation times of the order of 5 and  $20\ \mu\text{s}$ , respectively, in the temperature range close to  $T_N$ , our data are marked by large error bars in this temperature region and an accurate determination of  $T_N$  via  $1/T_1$  is difficult. From the overall temperature dependence of the spin-lattice relaxation rate  $T_N$  was determined to be about  $(2.5 \pm 0.2)\ \text{K}$  at 2 T.

While the longitudinal nuclear magnetization is well described by the standard expression of a nuclear spin  $I$

$= 1/2$  with a single  $T_1$  component for  $^{207}\text{Pb}$  and for all field directions, for  $^1\text{H}$  an additional  $T_1$  component with a very short spin-lattice relaxation time of the order of  $\sim 10\ \mu\text{s}$  needs to be taken into account for the whole temperature range for  $H \parallel b$ .<sup>55</sup> Although it cannot be ruled out completely that the short  $T_1$ -component arises from either impurities in the sample or from a  $^1\text{H}$  background signal from e.g. teflon outside the coil, both its qualitatively similar temperature dependence as well as its complete absence for the other two directions, strongly hint towards an intrinsic signal. However, the origin of this very fast-relaxing component for  $H \parallel b$  is not clear up to now and needs further investigation. Thus, we solely concentrate on the single, longer  $T_1$  component in the following.

Overall, as temperature is lowered, for both nuclei one finds a strong increase in  $1/T_1(T)$  with a sharp peak at  $T_N \approx 2.5(2)\ \text{K}$ , below which the spin-lattice relaxation rate decreases again as shown for all three principle directions (Fig. 12). This sharp peak is indicative of a transition into the 3D ordered state. The divergence of the relaxation rate  $1/T_1$  due to the transition at  $\sim 2.5\ \text{K}$  makes a further comparison to any low-dimensional (1D,

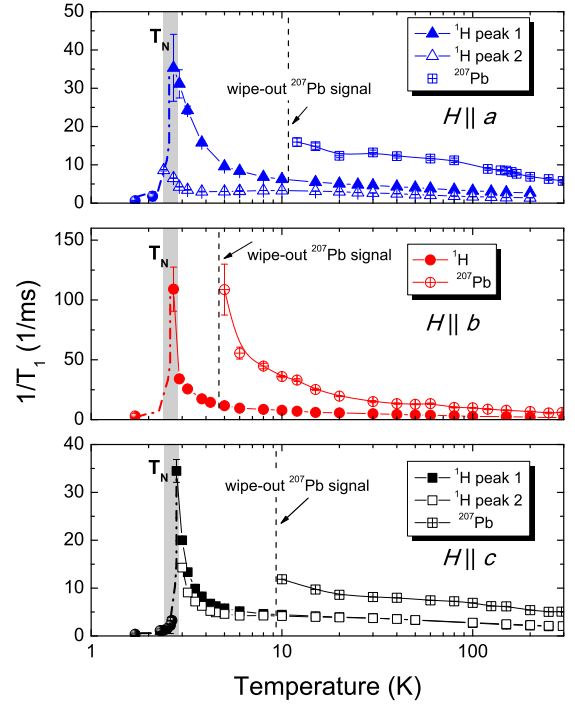


FIG. 12: (Color online) The spin-lattice relaxation rate,  $1/T_1$ , of  $\text{PbCuSO}_4(\text{OH})_2$  as function of temperature determined in an external field of 2 and 4 T for  $^1\text{H}$  and  $^{207}\text{Pb}$ , respectively. While the  $^{207}\text{Pb}$ -NMR signal was wiped out at low temperatures due to very short spin-spin and spin-lattice relaxation rates, the  $^1\text{H}$ -NMR signal could be observed in the whole temperature regime. Note that the average  $1/T_1$ -value has been extracted for  $H \parallel b$  due to overlapping  $^1\text{H}$ -NMR lines. The lines are guides to the eyes.

2D) models in the paramagnetic regime difficult, as it masks the quasi-1D behavior of linarite at low temperatures even above  $T_N$ . However, it is crucial to emphasize that the  $^1\text{H}$ -NMR investigations in the 3D ordered state have shown a sharp splitting into a multi-peak pattern, which is consistent with a non-trivial antiferromagnetic alignment of the Cu-spins below  $T_N$ . Correspondingly, the  $1/T_1$  data below  $T_N$ , shown in Fig. 12 as closed circles, reflect the average value of  $1/T_1$  for all lines with the small distribution of values marked by error bars.

## VI. THEORETICAL ANALYSIS - ASSIGNMENT OF EXCHANGE INTEGRALS

### A. Saturation fields and Curie-Weiss temperature

As a starting point, we assume at first that the interchain interaction is weak and that the inchain interaction (frustration) obeys the rigorous two-magnon bound state condition<sup>14</sup>  $\alpha > \alpha_{3c} = 0.3676776$ , i.e., it is within the quadrupolar region at the saturation field. Then, using the experimental value for the Curie-Weiss temperature  $\Theta_{\text{CW}} \approx 0.5|J_1|(1 - \alpha) \approx 27$  K, reported above, the estimated 1D saturation field of about  $H_s^a \approx 5.5$  T ( $H_{c3}$ , see Fig. 3), and the  $g$ -factor for  $H \parallel a$ , i.e.,  $g_a = 2.34$  (see Sect. IV), we obtain for the ratio  $r$  of the former quantities for the  $a$  direction

$$r = \frac{\Theta_{\text{CW}}}{g\mu_B H_s} = \frac{1 - \alpha^2}{4\alpha^2 + 2\alpha - 1} \approx 3.122575. \quad (6)$$

Note, that the last equation is a rigorous relation valid in the commensurate<sup>14,56</sup> 1D quadrupolar phase (QP) of the adopted spin model. Inverting Eq. (6), we obtain for the frustration ratio

$$\alpha(r) = \frac{\sqrt{5 + 5/r + 1/r^2} - 1}{4 + 1/r} \approx 0.36784 \quad (7)$$

still in the quadrupolar phase, although very close to the border to the octupolar phase at  $\alpha_{3c}$ . From  $\Theta_{\text{CW}}$  we obtain  $J_1 = -85.4$  K and  $J_2 = 31.4$  K.

In the opposite limit of strong enough antiferromagnetic interchain coupling, where multipolar effects disappear,<sup>39</sup> the former can be described at least approximately by the well-known one-magnon theory in the case of separable in-chain and interchain contributions to the total 3D (2D) saturation field.<sup>14</sup> As a result one arrives at

$$r = 0.5 \frac{1 - \alpha - \beta}{2\alpha - 1 + 0.125/\alpha}, \quad (8)$$

$$\alpha = \frac{0.5}{4r + 1} \left[ 2r + 1 - 0.5\rho + \sqrt{(3 - 2\rho)r + (1 - 0.5\rho)^2} \right] \approx 0.3639, \quad (9)$$

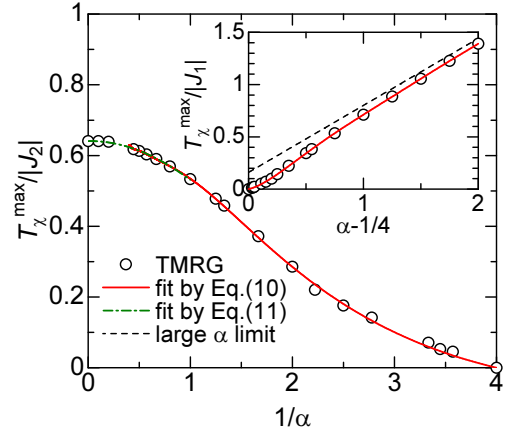


FIG. 13: (Color online) Maximum position  $T_\chi^{\text{max}}$  of the spin susceptibility  $\chi(T)$  measured in units of  $J_2$  as a function of  $1/\alpha$ , i.e., viewing the  $J_1$ - $J_2$  model as an equivalent realization of two interpenetrating *interacting* AFM Heisenberg chains. In the inset the maximum position  $T_\chi^{\text{max}}$  of  $\chi(T)$  measured in units of  $|J_1|$  vs. the frustration parameter  $\alpha$  according to DMRG calculations is shown (see text). The broken line describes the asymptotic curve  $T_\chi^{\text{max}} = 0.641J_2 \equiv 0.641\alpha|J_1|$ , well known from the Bethe-Ansatz-based solution for the unfrustrated AFM spin-1/2 Heisenberg chain.<sup>57</sup>

where  $\beta$  denotes the 2D interchain coupling in the basal plane measured in units of  $|J_1|$  and  $\rho = H_s^{3D}/H_s^{1D} - 1 \approx 0.3819$  is given by the ratio of the 3D(2D) and the 1D saturation fields, 7.6 T and 5.5 T, respectively, and the experimental value  $r = 3.122575$  has been used. These numbers result in  $J_1 = -86.7$  K and  $J_2 = 31.6$  K. Notice that the obtained value  $\alpha$  is very close to the "two-magnon-value" estimated above and the value obtained from the analysis of the magnetization measurements (see Fig. 14).

### B. Spin susceptibility and magnetization curve

Noteworthy, from the maximum position of the spin susceptibility at  $T_\chi^{\text{max}} = 4.9 \pm 0.3$  K in units of  $J_2$  or  $|J_1|$  (Fig. 13) we can also estimate an  $\alpha$ -value for our compound. Here,  $T_\chi^{\text{max}}$  is described with high precision by

$$\frac{T_\chi^{\text{max}}(\alpha)}{|J_1|} = \sum_{m=1}^6 A_m \left( \alpha - \frac{1}{4} \right)^m \quad \text{for } 9/4 \geq \alpha \geq 1/4, \quad (10)$$

with  $A_1 = 0.2778$ ,  $A_2 = 1.7055$ ,  $A_3 = -2.559$ ,  $A_4 = 1.8487$ ,  $A_5 = -0.6499$ , and  $A_6 = 0.0891$ .

The expression given by Eq. (10) has been obtained from a fit of our TMRG-data for  $\chi(T)$  for strong and intermediate coupling. We note that Eq. (10) also describes the experimental situation and parametrizations suggested for  $\text{Li}_2\text{ZrCuO}_4$  with  $\alpha = 0.3$ <sup>34</sup> as well as for



LiVCuO<sub>4</sub> with  $\alpha = 0.75$ .<sup>39,58</sup> In the opposite weak-coupling limit it is convenient to expand  $T_\chi^{\max}$  around the limiting point of decoupled interpenetrating AFM Heisenberg chains in powers of  $1/\alpha = |J_1|/J_2$ :

$$\frac{T_\chi^{\max}(\alpha)}{J_2} = 0.641 - \sum_{m=2}^5 \frac{D_m}{\alpha^m}, \quad \text{for } \alpha \geq 1, \quad (11)$$

with  $D_2 = 0.0034$ ,  $D_3 = 0.499$ ,  $D_4 = -0.669$ , and  $D_5 = 0.281$ .

For linarite, Eq. (10) yields somewhat larger values for the same  $\alpha$ , namely  $J_1 = -107.5$  K and  $J_2 = 39.5$  K. We ascribe this difference to the presence of an antiferromagnetic interchain coupling ignored in the former estimation and an uncertainty in the determination of  $\Theta_{\text{CW}}$ . (Note that  $T_\chi^{\max}$  is not affected by the interchain coupling within the random phase approximation adopted for its treatment at variance to the Curie-Weiss temperature  $\Theta_{\text{CW}}$ .)

A completely different situation has been suggested by Y. Yasui *et al.* [22]. These authors arrived at a  $T_\chi^{\max} \approx 3.8$  to 5 K somewhat lower than our values but at a *negative*  $\Theta_{\text{CW}} \approx -4$  K,  $J_1 = (-13 \pm 3)$  K, and an NNN exchange integral  $J_2 = (21 \pm 5)$  K, yielding a frustration ratio  $\alpha = 1.6$  belonging to the weak-coupling region. Adopting their  $\alpha$ -value and using their experimental  $T_\chi^{\max}$  of about 5 K (see inset in Fig. 2 of Ref. 22), one would arrive at  $J_2 \approx 8$  K and at  $J_1 \approx -5.2$  K, which is inconsistent with  $(21 \pm 5)$  K and  $(-13 \pm 3)$  K, respectively, claimed before.

Next, we checked these preliminary values of the in-chain exchange integrals by additionally describing the low- and intermediate-field magnetization data at  $T = 1.8$  K for the  $a_\perp$  direction (Fig. 14). The high-field region has not been taken into account due to an additional phase transition of yet unknown nature at low temperatures. The best fit at low fields is obtained for  $\alpha \sim 0.365$ . Then, the corresponding  $J_1$ -value consistent with a 1D saturation field of  $H_s = 5.5$  T becomes  $J_1 = -89.5$  K. These values are in accord with the values estimated above. Therefore they might be regarded as first realistic phenomenological values despite the ignored but certainly present weak interchain and spin-anisotropy effects, only briefly discussed below as an outlook for future studies.

Finally, the analysis of the spin-susceptibility data nicely confirms the above results (Fig. 15). In the analysis the obtained experimental parameters for the  $g$ -factor and the Curie-Weiss constant have been used. The best matching between experimental data and theoretical calculations results in magnetic exchange parameters  $J_1 = -94$  K and  $J_1 = -101.2$  K ( $\alpha = 0.36$ ) for the  $a$  and  $b$  direction, respectively, again highlighting the magnetic anisotropy in our system.

In summary, within the simplest isotropic spin chain model our values for  $J_1 \approx -97 \pm 10$  K and  $J_2 \approx 36 \pm 4$  K exceed significantly those determined previously from fits

of the  $T$ -dependent susceptibility in the high- $T$  regime, where only  $J_1 = -30$  K ( $-13$  K) and  $J_2 = 15$  K ( $21$  K), respectively, have been extracted.<sup>22,33</sup> In addition, we also found a considerably smaller frustration parameter  $\alpha \approx 0.37$  instead of 0.5 and 1.62, respectively,<sup>22,33</sup> which puts linarite closer to the 1D critical point at 0.25 with consequences for a weaker critical antiferromagnetic interchain coupling for ordered multipolar phases at  $T = 0$ .<sup>18</sup> The former might be masked by non-negligible impurity contributions in accord with a 3D analysis of the anisotropic susceptibility data (see below).

### C. Aspects of interchain coupling and symmetric exchange anisotropy for $\chi(T)$

The interchain coupling (IC) has been taken into account in the frame of the frequently used random phase approximation (RPA):<sup>57,59</sup>

$$\chi_{3D}(T) \approx \frac{\chi_{1D}}{1 + k\chi_{1D}(T)}, \quad (12)$$

where the one-dimensional susceptibility,  $\chi_{1D}(T)$ , has been calculated applying the TMRG-method, the interchain coupling  $k = (g/2)^2 \sum J_{ic}/|J_1|$  yields a temperature independent single parameter and the summation runs over all interchain couplings. The fits to the data shown in Fig. 15 result in slightly different IC parameters  $k = -0.081$  and  $-0.1$  for the  $a$  and  $b$  direction, respectively, corresponding to a weak FM IC of a few K. In principle, a small underestimation of  $\chi(T)$  within its maximum region can be removed adopting also an impurity contribution described by a Curie or a Curie-Weiss law as frequently used in the literature for other quasi-1D compounds (see e.g. Refs. 57,60). Despite the uncontrolled deviations introduced by the RPA, this way, the

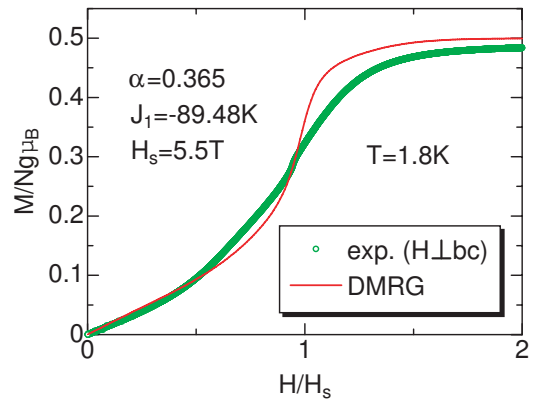


FIG. 14: (Color online) Fit for the magnetization vs. external field of PbCuSO<sub>4</sub>(OH)<sub>2</sub> at  $T = 1.8$  K and for  $H \parallel a_\perp$ .

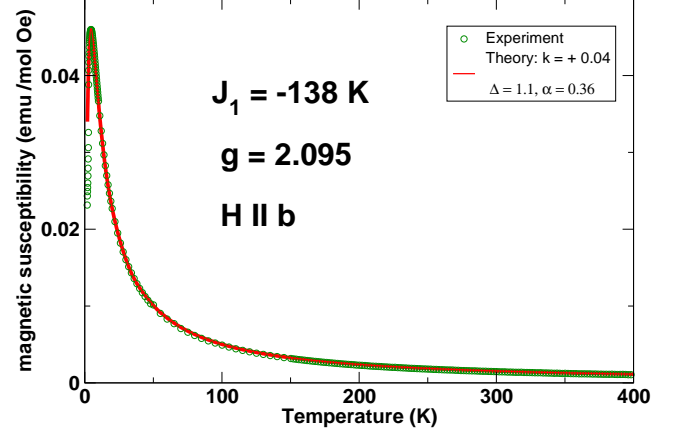
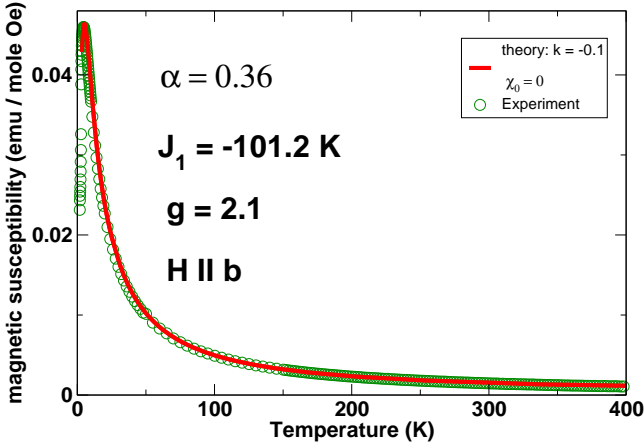
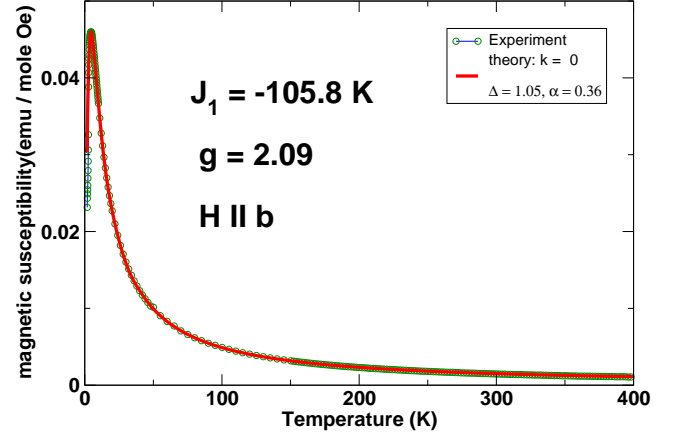
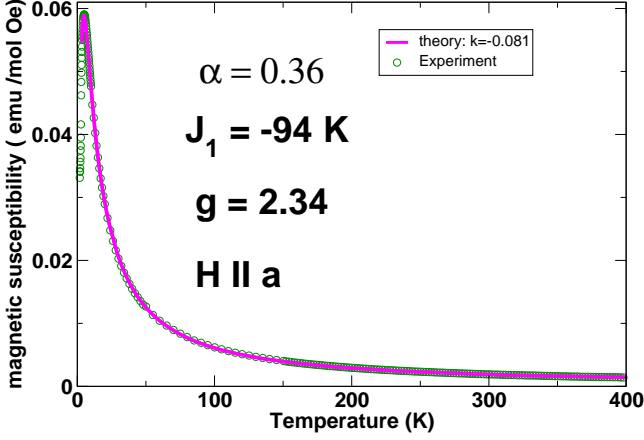


FIG. 15: (Color online) Analysis of the magnetic susceptibility,  $\chi(T)$ , within the isotropic  $J_1$ - $J_2$  model. The fitted solid lines result in slightly different IC parameters  $k = -0.081$  to  $-0.1$  (see text) corresponding to a weak FM IC of a few K. (a)  $H \parallel a$ , (b)  $H \parallel b$  axis. The  $g$ -factors are taken from Sect. IV.

determination of the interchain coupling is not unique and a (sizable) impurity contribution might mask weak antiferromagnetic interchain interactions.

A weak AFM IC of the order of  $J_{ic} \approx 4$  K follows also from the positive difference between the estimated 3D saturation fields and its 1D counter part of  $\approx 6$  T.<sup>14</sup> Alternatively, the high-field magnetization should be affected significantly by changed exchange integrals in the new high-field phase observed above  $\sim 6$  T. Inelastic neutron data such as in Ref. [61] might be useful to achieve a more precise assignment of the details such as the principle nature of the interchain coupling in our compound.

Due to the increase of a possible, small impurity contributions with decreasing  $T$  in our compound, the maximum positions of the impurity corrected susceptibilities

FIG. 16: (Color online) Magnetic susceptibility for a magnetic field applied along the suggested easy-axis ( $b$  axis) fitted within the 1D anisotropic  $J_1$ - $J_2$  model based on TMRG calculations supplemented by zero (upper panel) and finite antiferromagnetic (lower panel) interchain interactions treated in the RPA. The adopted easy-axis anisotropy is measured by the dimensionless parameter  $\Delta > 1$  (see text).

are upshifted by a few tenths of a K. Naturally the effect is largest for the  $b$ -axis susceptibility (shift  $\sim 0.5$  K). Nevertheless, a significant anisotropy remains also for these "corrected" susceptibilities which points together with the obtained largest exchange integral  $J_1$  for the  $b$  axis to a corresponding easy-axis assignment. To improve further the theoretical analysis, a detailed consideration of an anisotropic  $J_1$ - $J_2$  model would be desirable which, however, is outside the scope of the present paper. For a first estimate see Fig. 16 and the short discussion given below.

Noteworthy, the quality of the fits can be improved without adopting a Curie-Weiss like impurity contribution, if instead a model with symmetric exchange anisotropy is applied. According to previous theoretical investigations of edge-shared cuprate chains with a ferromagnetic nearest neighbor exchange coupling, an easy-axis exchange anisotropy is expected.<sup>62,63</sup> Therefore the first term in the isotropic spin-Hamiltonian should be replaced by

$$J_1 \vec{S}_i \vec{S}_{i+1} \rightarrow J_1 (S_i^x S_{i+1}^x + S_i^z S_{i+1}^z) + J_1 \Delta_1 S_i^y S_{i+1}^y,$$

with  $\Delta_1 > 1$  (see Fig. 16). Such an easy-axis exchange anisotropy affects significantly the low-temperature behavior of  $\chi(T)$  and the saturation field in the low  $\alpha$ -region of interest. Following Ref. 14, but ignoring weak anisotropy effects for the next-nearest neighbor exchange (i.e., setting  $\Delta_2 = 1$ ), we rewrite the leading term in the expression for the 1D saturation field valid in the two-magnon case at weak interchain coupling as

$$g\mu_B H_s(\Delta_1) = |J_1| (2\alpha - \Delta_1 + 0.5\Delta_1^2 / [\Delta_1 + \alpha]), \quad (13)$$

and analogously in the one-magnon case:

$$g\mu_B H_s(\Delta_1) = |J_1| (2\alpha - \Delta_1 + 0.125/\alpha). \quad (14)$$

The effect of the easy-axis anisotropy under consideration on the in-chain exchange coupling  $J_1$  is illustrated in Fig. 17 for the case we are interested in here, namely, when one extracts the  $J_1$ -value from a given experimental saturation field  $H_s$ .

In the presence of an antiferromagnetic interchain coupling the enhancement effect for the corresponding renormalization of  $J_1$  is a bit less dramatic but nevertheless significant. Such a behavior is in accord with a similar effect found for the magnetic susceptibility data fitted by the isotropic and the anisotropic model as shown in Figs. 15,16. Thus, within such a scenario the observed increase of  $|J_1|$  by more than 30 K becomes rather natural. These results are in reasonable agreement with recent L(S)DA+ $U$  calculations, based on a refined crystallographic structure of  $\text{PbCuSO}_4(\text{OH})_2$  including the corrected proton positions,<sup>38</sup> see below. Note that the range of validity of the expression given by Eq. (13) with respect to the formation of three-magnon bound states is under investigation at present. However, qualitatively the same behaviour is also expected for the octupolar three-magnon and other multipolar phases. A systematic study of exchange anisotropy effects including also  $J_2$  as well as the interchain coupling is postponed for a future study.

#### D. Density functional theory: L(S)DA + $U$

To probe our new parameter set with respect to a microscopic picture, we carried out DFT band structure calculations within the LSDA+ $U$  scheme which takes into

account the strong Coulomb repulsion,  $U$ , at the Cu site. Since we observed a sizable dependence of the resulting exchange parameters from the H position,<sup>64</sup> our calculations are based on the recently refined crystal structure of Ref. 38. For a screened Coulomb repulsion  $U = 7$  eV, which is in the typical range of  $U$  values that were successfully applied to related Cu-O systems,<sup>36,61,65</sup> and the usual value of the Hund's rule coupling  $J = 1.0$  eV which enters the L(S)DA+ $U$  calculational scheme, we obtain a frustration ratio  $\alpha \approx 0.32$ . This value is in reasonable agreement with the value  $\alpha \approx 0.36$  derived from the experimental data (compare Tab. 1), in view of possible renormalizations due to a non-negligible spin-lattice coupling in the non-adiabatic limit or intermediate case and of possible quantum-effect caused by the zero-point motion of the light hydrogen nuclei ignored in all density functional approaches.

The resulting frustration ratio  $\alpha$  depends only moderately on  $U$  within the physically reasonable range between 5 and 8 eV (Fig. 18). The respective calculated exchange integrals ( $U = 7$  eV) are  $J_1 = -133$  K and  $J_2 = 42$  K. These numbers are in good agreement with the isotropic parts obtained within the easy-axis model for the fit of the magnetic susceptibility with  $H \parallel b$  reported

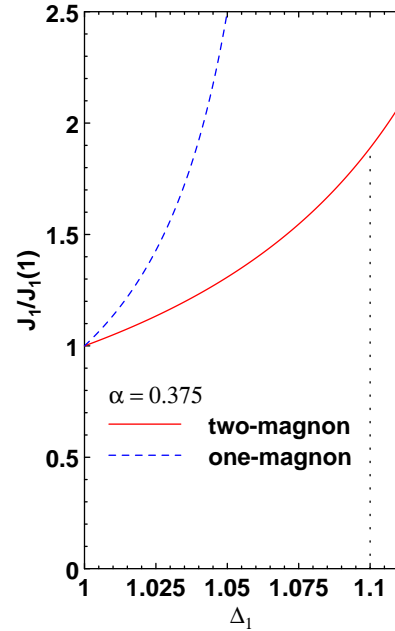


FIG. 17: (Color online) Value of the isotropic part of the ferromagnetic nearest-neighbor exchange integral  $J_1$  in units of the corresponding value in the isotropic model vs. the dimensionless anisotropy factor  $\Delta_1 \geq 1$  as derived from Eqs. (13) and (14).

above:  $-J_1 = 138$  K and  $J_2 = 49.7$  K. In other words, also the LSDA+ $U$  derived exchange integrals clearly support a scenario with significantly larger  $J$ -values compared to those proposed in Refs. 22,33. Taking into account the different interchain couplings  $J_{ic,0}$ ,  $J_{ic,1}$ , and  $J_{ic,2}$  (see Fig. 1) as well as the respective number of neighbors we can estimate an effective interchain coupling  $J_{ic} \sim 7$  K. This is also consistent with the analysis of  $\chi(T)$  within the easy-axis model which yields  $\approx 5$  K. A detailed electronic-structure study of the title compound under consideration, in particular its structural stability and the sizable dependence of the coupling parameters from the details of the crystal structure, will be published elsewhere.<sup>64</sup>

## VII. CONCLUSION

In conclusion, we have performed a detailed combined experimental and theoretical study of  $\text{PbCuSO}_4(\text{OH})_2$  in the paramagnetic regime in fields up to saturation. The saturation field, probed via magnetization studies at low temperatures, is anisotropic for the three principal crystallographic axes ranging between 7.6 and 10.5 T. ESR and NMR measurements further prove that the static susceptibility is dominated by the intrinsic spin susceptibility. The Knight shift as well as the broadening of the linewidth in the ESR and NMR data at elevated temperatures indicate a frustrated system with the onset of anisotropic magnetic correlations far above the magnetic ordering temperature,  $T_N = 2.75(5)$  K. Our experimen-

axis	$a$	$b$
$g$ (ESR)	2.34	2.1
$\Theta_{CW}$ (K)	27	27
$H_s$ (T) from 1D $M(H, T = 1.8\text{K})$	5.5	
$-J_1$ (K) (IHM, $\chi(T)$ )	94	101
$J_2$ (K), (IHM, $\chi(T)$ )	33.8	36.4
$-J_1$ (K) (IHM, $M(H)$ )	89.5	
$J_2$ (K) (IHM, $M(H)$ )	32.7	
$-J_1$ (K), (AHM)		138
$\alpha$ (IHM, $M(H)$ )	0.365	
$\alpha$ (AHM)		0.36
$-J_1$ (K), (LSDA+U)	133	133
$J_2$ (K), (LSDA+U)	42	42

TABLE I: Calculated magnetic exchange interactions  $J_1$  and  $J_2$  along the chain using a 1D approach based on the analysis of saturation fields at  $T = 0$ , low- and intermediate field magnetization data within the DMRG, and LSDA +  $U$  calculations, together with the experimental values for the  $g$ -factor,  $H_s$ , and  $\Theta_{CW}$  of  $\text{PbCuSO}_4(\text{OH})_2$ ; for details see text. The abbreviations IHM and AHM denote isotropic and anisotropic Heisenberg model, respectively.

tal data are analyzed both in 1D as well as quasi-1D approaches based on DMRG and hard-core boson calculations, yielding values for the exchange interactions  $J_1 \sim -100$  K and  $J_2 \sim 36$  K along the chain as well as a weak interchain coupling of a few K, leaving room for a quadrupolar phase (*i.e.*, spin nematics) in experimentally accessible magnetic fields.

In view of the small absolute value of the saturation field and the rich manifold of field-induced phases (particularly along the chain direction),  $\text{PbCuSO}_4(\text{OH})_2$  reveals itself as a promising material for additional investigations in the future. In particular, linarite possibly realizes a prototype for investigating the recently predicted spin multipolar order close to the saturation field,  $H_s$ , of such frustrated "ferromagnetic" spin-chain compounds.

From a theoretical point of view, such a systematic study of one compound on high-quality single crystals might be very helpful for a future unified theory of frustrated edge-shared cuprates in order to understand what is really puzzling in each compound of that increasing family and what some of these compounds have in common. In particular, the question which of their properties can be used best for the determination of a specific model parameter from experimental data seems to be important.

## Acknowledgements

We acknowledge fruitful discussions with R. Giraud, H.-J. Grafe, C. Berthier, R. Kuzian, J. Richter and R. Zinke. We thank O. Kataeva, S. Partzsch and J. Geck for the x-ray characterization of the samples and S. Gaß for technical support. We are particularly thankful to G. Heide and M. Gäbelein from the *Geoscientific Collections* for supplying us with their linarite crystal of *origin 1*. F. Pfeiffer is acknowledged for supplying us with the linarite samples of *origin 2*. This work has been supported by the DFG through the grants: WO 1532/3-1, SU 229/10-1, FOR 912 and DR 269/3-1. Part of this work has been supported by EuroMagNET under the EU contract no. 228043.

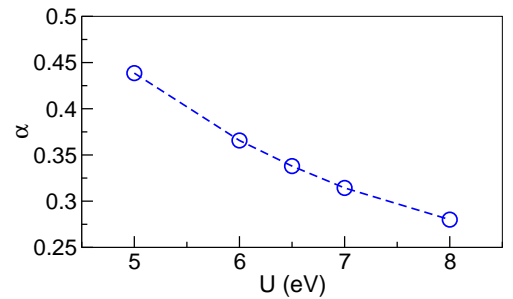


FIG. 18: Frustration parameter vs.  $U$  from L(S)DA+ $U$  for  $\text{PbCuSO}_4(\text{OH})_2$ . The Hund's rule exchange at Cu sites has been fixed at  $J = 1.0$  eV for all calculations.



- <sup>1</sup> Eds. U. Schollwöck, J. Richter, D.J.J. Farnell, and R.F. Bishop, *Quantum Magnetism, Lecture Notes in Physics* vol. **645**, Springer, Berlin Heidelberg (2004).
- <sup>2</sup> O. Vyaselev, M. Takigawa, A. Vasiliev, A. Oosawa, and H. Tanaka, *Phys. Rev. Lett.* **92**, 207202 (2004).
- <sup>3</sup> M. Clémancey, H. Mayaffre, C. Berthier, M. Horvatić, J.-B. Fouet, S. Miyahara, F. Mila, B. Chiari, and O. Piovesana, *Phys. Rev. Lett.* **97**, 167204 (2006).
- <sup>4</sup> N. Laflorencie, and F. Mila, *Phys. Rev. Lett.* **102**, 060602 (2009).
- <sup>5</sup> M. Jaime, V.F. Correa, N. Harrison, C.D. Batista, N. Kawashima, Y. Kazuma, G.A. Jorge, R. Stein, I. Heinmaa, S.A. Zvyagin, Y. Sasago, and K. Uchinokura, *Phys. Rev. Lett.* **93**, 087203 (2004).
- <sup>6</sup> S. E. Sebastian, N. Harrison, C.D. Batista, L. Balicas, M. Jaime, P.A. Sharma, N. Kawashima, and I.R. Fisher, *Nature* **441**, 617 (2006).
- <sup>7</sup> T. Giamarchi, C. Rüegg, and O. Tchernyshyov, *Nat. Phys.* **4**, 198 (2008).
- <sup>8</sup> S. Krämer, R. Stern, M. Horvatić, C. Berthier, T. Kimura, and I.R. Fisher, *Phys. Rev. B* **76**, 100406(R) (2007).
- <sup>9</sup> M. E. Zhitomirsky, and H. Tsunetsugu, *EPL* **92**, 3701 (2010).
- <sup>10</sup> L.E. Svistov, T. Fujita, H. Yamaguchi, S. Kimura, K. Omura, A. Prokofiev, A.I. Smirnov, Z. Honda, and M. Hagiwara, *Pis'ma ZhETF (JETP Lett.)* **93**, 24(21) (2011).
- <sup>11</sup> M. Sato, T. Momoi, and A. Furusaki, *Phys. Rev. B* **79**, 060406(R) (2009).
- <sup>12</sup> M. Sato, T. Hikiyara, and T. Momoi, *Phys. Rev. B* **83**, 064405 (2011).
- <sup>13</sup> L. Kecke, T. Momoi, and A. Furusaki, *Phys. Rev. B* **76**, 060407(R) (2007).
- <sup>14</sup> R. O. Kuzian, and S.-L. Drechsler, *Phys. Rev. B* **75**, 024401 (2007).
- <sup>15</sup> T. Hikiyara, L. Kecke, T. Momoi, and A. Furusaki, *Phys. Rev. B* **78**, 144404 (2008).
- <sup>16</sup> A. Läuchli, J. Sudan, and A. Lüscher, *J. of Phys.: Conf. Ser.* **145**, 012057 (2009).
- <sup>17</sup> D.V. Dmitriev, and V.Ya. Krivnov, *Phys. Rev. B* **79**, 054421 (2009).
- <sup>18</sup> S. Nishimoto, S.-L. Drechsler, R. Kuzian, J. Richter, and J. van den Brink, *arXiv:1005.5500*, unpublished.
- <sup>19</sup> E. Plekhanov, A. Avella, and F. Mancini, *Europ. Phys. J. B* **77**, 381 (2010).
- <sup>20</sup> M. Kumar, Z.G. Soos, D. Sen, and S. Ramasesha, *Phys. Rev. B* **81**, 104406 (2010).
- <sup>21</sup> J. Sirker, V.Y. Krivnov, D.V. Dmitriev, A. Herzog, S. Nishimoto, S.-L. Drechsler, and J. Richter, *arXiv:1106.1008*, unpublished.
- <sup>22</sup> Y. Yasui, M. Sato, and I. Terasaki, *J. Phys. Soc. Jpn.* **80**, 033707 (2011).
- <sup>23</sup> M. Hase, H. Kuroe, K. Ozawa, O. Suzuki, H. Kitazawa, G. Kido, and T. Sekine, *Phys. Rev. B* **70**, 104426 (2004).
- <sup>24</sup> M. Enderle, C. Mukherjee, B. Fak, R.K. Kremer, J.-M. Broto, H. Rosner, S.-L. Drechsler, J. Richter, J. Malek, A. Prokofiev, W. Assmus, S. Pujol, J.-L. Raggazzoni, H. Rakoto, M. Rheinstädter, and H.M. Ronnow, *Europhys. Lett.* **70**, 237 (2005).
- <sup>25</sup> N. Büttgen, H.-A. Krug von Nidda, L.E. Svistov, L.A. Prozorova, A. Prokofiev, and W. Assmus, *Phys. Rev. B* **76**, 014440 (2007).
- <sup>26</sup> N. Büttgen, W. Kraetschmer, L.E. Svistov, L.A. Prozorova, and A. Prokofiev, *Phys. Rev. B* **81**, 052403 (2010).
- <sup>27</sup> S.-L. Drechsler, J. Richter, A.A. Gippius, A. Vasiliev, A.A. Bush, A.S. Moskvina, J. Málek, Yu. Prots, W. Schnelle, and H. Rosner, *Europhys. Lett.* **73**, 83 (2006).
- <sup>28</sup> T. Masuda, A. Zheludev, A. Bush, M. Markina, and A. Vasiliev, *Phys. Rev. Lett.* **92**, 177201 (2004).
- <sup>29</sup> T. Masuda, A. Zheludev, B. Roessli, A. Bush, M. Markina, and A. Vasiliev, *Phys. Rev. B* **72**, 014405 (2005).
- <sup>30</sup> S. Park, Y.J. Choi, C.L. Zhang, and S.-W. Cheong, *Phys. Rev. Lett.* **98**, 057601 (2007).
- <sup>31</sup> S. Seki, Y. Yamasaki, M. Soda, M. Matsuura, K. Hirota, and Y. Tokura, *Phys. Rev. Lett.* **100**, 127201 (2008).
- <sup>32</sup> G. Kamieniarz, M. Bielski, G. Szukowski, R. Szymczak, S. Dyeyev, and J.-P. Renard, *Comp. Phys. Comm.* **147**, 716 (2002).
- <sup>33</sup> M. Baran, A. Jedrzejczak, H. Szymczak, V. Maltsev, G. Kamieniarz, G. Szukowski, C. Loison, A. Ormeci, S.-L. Drechsler, and H. Rosner, *phys. stat. sol. (c)* **3**, 220 (2006).
- <sup>34</sup> S.-L. Drechsler, O. Volkova, A.N. Vasiliev, N. Tristan, J. Richter, M. Schmitt, H. Rosner, J. Málek, R. Klingeler, A.A. Zvyagin, and B. Büchner, *Phys. Rev. Lett.* **98**, 077202 (2007).
- <sup>35</sup> E. Vavilova, A.S. Moskvina, Y.C. Arango, A. Sotnikov, S.-L. Drechsler, R. Klingeler, O. Volkova, A.N. Vasiliev, V. Kataev, and B. Büchner, *EPL* **88**, 27001 (2009).
- <sup>36</sup> M. Schmitt, J. Málek, S.-L. Drechsler, and H. Rosner, *Phys. Rev. B* **80**, 205111 (2009).
- <sup>37</sup> S.-L. Drechsler, J. Richter, R. Kuzian, J. Málek, N. Tristan, B. Büchner, A.S. Moskvina, A.A. Gippius, A. Vasiliev, O. Volkova, A. Prokofiev, H. Rakoto, J.M. Broto, W. Schnelle, M. Schmitt, A. Ormeci, C. Loison, and H. Rosner, *J. Mag. Magn. Mat.* **316**, 306 (2007).
- <sup>38</sup> P.F. Schofield, C.C. Wilson, K.S. Knight, and C.A. Kirk, *The Canadian Mineralogist* **47**, 649 (2009).
- <sup>39</sup> S. Nishimoto, S.-L. Drechsler, R. Kuzian, J. Richter, J. Málek, M. Schmitt, J. van den Brink, and H. Rosner, *arXiv:1105.2810v1* (2011), unpublished; see Fig. 3 therein.
- <sup>40</sup> C. Golze, A. Alfonsov, R. Klingeler, B. Büchner, V. Kataev, C. Mennerich, H.-H. Klauss, M. Goiran, J.-M. Broto, H. Rakoto, S. Demeshko, G. Leibel, and F. Meyer, *Phys. Rev. B* **73**, 224403 (2006).
- <sup>41</sup> R.J. Bursill, T. Xiang, and G.A. Gehring, *J. Phys.: Condens. Matter* **8**, L583 (1996).
- <sup>42</sup> X. Wang and T. Xiang, *Phys. Rev. B* **56**, 5061 (1997).
- <sup>43</sup> N. Shibata, *J. Phys. Soc. Jpn* **66**, 2221 (1997).
- <sup>44</sup> S.R. White, *Phys. Rev. Lett.* **69**, 2863 (1992).
- <sup>45</sup> H.-J. Koo, C. Lee, M.-H. Whangbo, G.J. McIntyre, and R.K. Kremer, *Inorg. Chem.* **50**, 3582 (2011).
- <sup>46</sup> K. Koepnik and H. Eschrig, *Phys. Rev. B* **59**, 1743 (1999).
- <sup>47</sup> H. Eschrig, K. Koepnik, and I. Chaplygin, *J. Solid State Chem.* **176**, 482 (2003).
- <sup>48</sup> J. P. Perdew and Y. Wang, *Phys. Rev. B* **45**, 13244 (1992).
- <sup>49</sup> Due to technical reasons (sample mounting and sample space) the field was applied perpendicular to the (*bc*) plane rather than parallel to the *a* axis for the magnetization measurements. However, since the angular dependence of *M* is expected to be proportional to  $\cos \beta$  ( $\beta$  = angle between *H* and the principal crystallographic direction), a

misalignment of about  $12^\circ$  with respect to the  $a$  axis only results in a change of  $M$  by less than 3%.

<sup>50</sup> B. Willenberg *et al.*, unpublished.

<sup>51</sup> Note that resonance fields are as measured and not corrected by the temperature-dependent resonance frequency of the cavity, which can cause a shift of the order of 10 mT from 100 K to 300 K.

<sup>52</sup> H. Benner, and J.P. Boucher, Ed. L.J. de Jongh, Magnetic Properties of layered transition metal compounds, vol. 9, Kluwer Academics Publ. (1990).

<sup>53</sup> Y. Tazuke, K. Nagata, J. Phys. Soc. Jpn. **38**, 4 (1975).

<sup>54</sup> The practically unavoidable simultaneous excitation of the two inequivalent  $^1\text{H}$ -NMR lines at high temperatures prevented an exact determination of the NMR shift in the high-temperature regime above 200-250 K. Therefore, only  $^{207}\text{Pb}$ -NMR was conducted in this temperature regime.

<sup>55</sup> Since such a short spin-lattice relaxation time is far too small to be determined quantitatively considering the deadtime of our spectrometer, we used a saturation recovery sequence with an echo subsequence at the end for the determination of the spin-lattice relaxation time for  $H \parallel b$ . In this way, the short  $T_1$  component was revealed by a small non-zero magnetization component for  $\tau_{var} \rightarrow 0$  and could be neglected in the following analysis of the second, larger  $T_1$  component.

<sup>56</sup> Thereby the bound two-magnon state bears a moment  $\pi/a$ . The lower bound for the corresponding  $\alpha$  value amounts to about  $\alpha_c \approx 0.37466105983527$ .<sup>14</sup> For  $\alpha_{c3} = 0.3676 \leq \alpha \leq \alpha_c$  an incommensurate two-magnon phase is expected, where the moment of the magnon pair is slightly downshifted from  $\pi/a$ . Just this happens for the  $\alpha$ -value obtained for linarite. However, due to the smooth transition between both these two-magnon phases the expected saturation field will be only slightly larger than the pre-

diction by the extrapolated simple analytic commensurate expression we have used. The situation is similar for the behavior near the border line between the incommensurate and commensurate phase discussed in Ref. 39 (see the inset in Fig. 5 and the corresponding EPAPS-supplementary part therein). For the purpose of a first estimate of  $\alpha$  such tiny differences might be ignored for the sake of simplicity. Hence, to avoid such problems we adopted in the illustrating Fig. 17, based on the analytical solution for the commensurate two-magnon case, a close but slightly higher  $\alpha$  value of  $0.375 > \alpha_c$ .

<sup>57</sup> D. Johnston in "Handbook of Magnetic Materials" (Ed. by K.H.J. Buschow) v. 10, Noth-Holland, Elsevier Amsterdam 1997.

<sup>58</sup> S.-L. Drechsler, S. Nishimoto, R.O. Kuzian, J. Málek, W.E.A. Lorenz, J. Richter, J. van den Brink, M. Schmitt, and H. Rosner, Phys. Rev. Lett. **106**, 219701 (2011).

<sup>59</sup> M. Bocquet, F.H.L. Essler, A.M. Tsvelik, and A.O. Gogolin, Phys. Rev. B **64**, 094425 (2001).

<sup>60</sup> R. Nath, A.V. Mahajan, N. Büttgen, C. Kegler, A. Loidl, and J. Bobroff, Phys. Rev. B **71**, 174436 (2005).

<sup>61</sup> W. E. A. Lorenz, R. O. Kuzian, S.-L. Drechsler, W.-D. Stein, N. Wizen, G. Behr, J. Málek, U. Nitzsche, H. Rosner, A. Hiess, W. Schmidt, R. Klingeler, M. Loewenhaupt, and B. Büchner, Europhys. Lett. **88**, 37002 (2009).

<sup>62</sup> S. Tornow, O. Entin-Wohlman, and A. Aharony, Phys. Rev. B **60**, 10206 (1999).

<sup>63</sup> V. Yushankhai and R. Hayn Europhys. Lett. **47**, 116 (1999).

<sup>64</sup> M. Schmitt *et al.*, unpublished.

<sup>65</sup> M. D. Johannes, J. Richter, S.-L. Drechsler, and H. Rosner, Phys. Rev. B **74**, 174435 (2006).